ATLAS CONF Note

ATLAS-CONF-2022-026

4th April 2022

Measurement of substructure-dependent jet suppression in Pb+Pb collisions at 5.02 TeV with the ATLAS detector

The ATLAS Collaboration

Jet substructure modification and suppression are measured in Pb+Pb collisions at a nucleon-nucleon center-of-mass energy $\sqrt{s_{\mathrm{NN}}} = 5.02$ TeV with respect to pp collisions at $\sqrt{s} = 5.02$ TeV with the ATLAS detector at the Large Hadron Collider. The Pb+Pb data were collected in 2018 with an integrated luminosity of 1.72 nb^{-1}, while the pp data were collected in 2017 with an integrated luminosity of 260 pb^{-1}. Jets used in this analysis are clustered using the anti-k_t algorithm with a radius parameter $R = 0.4$. The jet constituents, defined by both tracking and calorimeter information, are used to define the angular scale r_{g} of the first hard splitting inside the jet by reclustering them using the Cambridge-Aachen algorithm and employing the soft drop grooming technique with parameters $\beta = 0$ and $z_{\mathrm{cut}} = 0.2$. The jet nuclear modification factor, R_{AA}, used to characterize the jet suppression in Pb+Pb collisions, is presented differentially in r_{g}, jet transverse momentum, and in intervals of collision centrality. The R_{AA} is observed to depend significantly on jet r_{g}, with the production of jets with the largest measured r_{g} found to be twice as suppressed compared to those with the smallest r_{g} in central Pb+Pb collisions. The R_{AA} values do not exhibit a strong variation with jet p_{T} in any of the r_{g} intervals. The r_{g} and p_{T} dependence of jet R_{AA} is qualitatively consistent with a picture of jet quenching arising from coherence and provides the most direct evidence in support of this approach.

ATLAS-CONF-2022-026
11 April 2022

1 Introduction

In ultra-relativistic heavy-ion collisions a hot and dense form of matter is produced known as the quark-gluon plasma (QGP). The temperatures attained by the fireball are such that quarks and gluons are no longer confined to their parent hadrons [1, 2]. Producing the QGP in the laboratory enables unique opportunities to study quantum chromodynamics (QCD). Experimental results from the Relativistic Heavy Ion Collider (RHIC) and the Large Hadron Collider (LHC) have established the interpretation that the system expands hydrodynamically. The remarkably small viscosity needed to describe the data suggests that this matter exhibits strong-coupling behavior on long distance scales [3]. In contrast, at short distance scales the interactions among quarks and gluons are expected to become weaker due to fact that QCD exhibits asymptotic freedom. It is not fully understood how such hydrodynamic behavior arises from the interactions among elementary quarks and gluons [4]. To address this challenge, the dynamics of the QGP must be characterized on a range of length scales.

Jets are highly collimated sprays of particles resulting from the point-like, hard scattering of quarks and gluons, collectively referred to as partons. Jets are produced at the earliest stages of the collision and become attenuated through the plasma, a phenomenon known as jet quenching [5, 6]. The energy loss suffered by a jet and the modification of its radiation pattern provide information on the plasma's microscopic structure. In the vacuum the scattered partons undergo copious radiation, and thus the modification of the jet evolution process in the QGP is inherently a multi-scale problem.

Techniques that rigorously define jet substructure and enable the identification of the hardest splitting in a jet's parton shower have been developed [7, 8]. The soft-drop grooming procedure [9], a generalization of the modified mass-drop tagger [8], shows a reduced sensitivity in theoretical calculations to the effects of initial state radiation, multi-parton interactions and non-perturbative contributions to substructure observables. As these effects typically contribute large uncertainties, mitigating their effects enables more rigorous comparisons with experimental data [10, 11]. The potential of such techniques to characterize jet substructure in heavy-ion collisions has also been recognized [12–14], and a first series of measurements have been performed indicating a slight modification of jet substructure variables in Pb+Pb collisions compared to pp results [15–18]. However these initial studies have not yet elucidated the relationship between the observed modifications and the energy loss of the jet.

Numerous measurements of jet quenching in heavy-ion collisions performed at RHIC and LHC [19, 20] typically have fallen into two categories: quantifying the total energy loss and studying the modification of the jet's radiation pattern. The rate of jets produced in central heavy-ion collisions at a given jet transverse momentum, $p_{\mathrm{T}}^{\mathrm{jet}}$, is observed to be reduced by approximately a factor of two compared to pp measurements [21–24]. Additionally, back-to-back dijet and photon/Z-jet pairs are observed to be less balanced in Pb+Pb collisions compared to those in pp measurements [25–28]. These measurements provide information on the total jet energy loss and its parametric dependence on the in-medium path length and flavor of the initiating parton, as well as constrain how energy loss may fluctuate on a jet-by-jet basis. Another class of measurements which studies the properties of quenched jets, typically through the particle momentum distributions within jets [29–32], is less sensitive to the energy loss but can directly access how the radiation pattern is modified. This class includes the current heavy-ion jet substructure measurements [15–18, 33] as the distributions of substructure quantities are normalized per jet. Currently missing from the experimental program are analyses that quantify energy loss in terms of a jet's radiation pattern.

A common theoretical framework for describing jet quenching is the coherence picture in which interference effects, crucial for determining the structure of the vacuum parton shower [34], become disrupted by the medium, resulting in energy loss in the form of additional radiation [35]. Recent studies have also shown an emergence of a critical angle in the first hard splitting of a jet, above which the jet loses energy incoherently, i.e. as multiple color entities [36–39]. This approach leads to the expectation that a wide jet with two prongs, each of which may act as a separate emitter of radiation, will lose more energy than a narrow jet which acts as a single source of radiation. More generally, jets with different substructures are expected to experience different amounts of energy loss based on the degree to which the medium resolves the jet and induces decoherence of its radiation pattern [12].

This note describes a measurement of jet suppression, which is a measure of the energy loss, as a function of the observed substructure of the jet. The measurements are based on 1.72 nb^{-1} of Pb+Pb collision data collected in 2018 and 260 pb^{-1} of pp collision data collected in 2017, both with $\sqrt{s_{\text{NN}}} = 5.02$ TeV. The jets are reconstructed from energy deposits in the ATLAS calorimeters with the anti-k_t algorithm with $R = 0.4$ [40] and by applying a subtraction procedure that removes the underlying event contribution to the jet kinematics on an event-by-event basis [21]. The soft-drop grooming procedure is applied with parameters $\beta = 0$ and $z_{\text{cut}} = 0.2$ to jet constituents formed from charged-particle tracks and calorimeter energy deposits. The substructure is quantified through r_{g}, the angle subtended by the subjets chosen using the soft-drop procedure to tag the first hard splitting of a jet. Jets which fail the soft-drop requirement are considered as single-prong jets and assigned $r_{\text{g}} = 0$. The per-event jet yields as a function of $p_{\text{T}}^{\text{jet}}$ and r_{g} are measured in four centrality classes, which characterize the overlap of the colliding nuclei in Pb+Pb collisions. The analogous differential cross-sections are measured in pp collisions, and the suppression is quantified through the nuclear modification factor, R_{AA}. The cross-sections, yields, and R_{AA} are reported for jets with $p_{\text{T}}^{\text{jet}} > 158$ GeV and $0 \leq r_{\text{g}} < 0.4$. The measured cross-sections and yields are unfolded to a particle-level phase space.

2 ATLAS Detector

The ATLAS experiment [41] at the LHC is a multipurpose particle detector with a forward–backward symmetric cylindrical geometry and a near-4π coverage in solid angle.[1] It consists of an inner tracking detector surrounded by a thin superconducting solenoid providing a 2 T axial magnetic field, electromagnetic and hadron calorimeters, and a muon spectrometer. The high-granularity silicon pixel detector covers the vertex region and typically provides four measurements per track, with the first hit typically in the insertable B-layer installed before Run 2 [42, 43]. It is followed by the silicon microstrip tracker which usually provides eight measurements per track. These silicon detectors are complemented by the transition radiation tracker (TRT), which enables radially extended track reconstruction up to $|\eta| = 2.0$.

The calorimeter system covers the pseudorapidity range $|\eta| < 4.9$. Within the region $|\eta| < 3.2$, electromagnetic calorimetry (EMCal) is provided by barrel and endcap high-granularity lead/liquid-argon (LAr) calorimeters, with an additional thin LAr presampler covering $|\eta| < 1.8$ to correct for energy loss in material upstream of the calorimeters. Hadronic calorimetry (HCal) is provided by the steel/scintillator-tile

[1] ATLAS uses a right-handed coordinate system with its origin at the nominal interaction point (IP) in the centre of the detector and the z-axis along the beam pipe. The x-axis points from the IP to the centre of the LHC ring, and the y-axis points upwards. Cylindrical coordinates (r, ϕ) are used in the transverse plane, ϕ being the azimuthal angle around the z-axis. The pseudorapidity is defined in terms of the polar angle θ as $\eta = -\ln\tan(\theta/2)$. Angular distance is measured in units of $\Delta R \equiv \sqrt{(\Delta\eta)^2 + (\Delta\phi)^2}$.

calorimeter, segmented into three barrel structures within $|\eta| < 1.7$, and two copper/LAr hadronic endcap calorimeters. The solid angle coverage is completed with forward copper/LAr and tungsten/LAr calorimeter modules (FCal), covering the forward regions of $3.1 < |\eta| < 4.9$. The zero-degree calorimeters (ZDC) consist of layers of alternating quartz rods and tungsten plates and are located symmetrically at $z = \pm 140$ m and cover $|\eta| \geq 8.3$. In Pb+Pb collisions, the ZDCs primarily measure "spectator" neutrons: neutrons that do not interact hadronically when the incident nuclei collide.

Events of interest are selected for recording and offline analysis by the first-level trigger (L1) system implemented in custom hardware, followed by selections made by algorithms implemented in software in the high-level trigger (HLT) [44].

An extensive software suite [45] is used for real and simulated data reconstruction and analysis, for detector operation, and for the trigger and data acquisition systems of the experiment. The events used in this analysis were selected by a jet trigger [44]. At L1, jet candidates were identified by applying a sliding window algorithm and selecting events with a minimum threshold of 30 GeV. These events were then passed to the high-level jet trigger, which uses a jet reconstruction and background subtraction procedure similar to that used in the offline analysis and requires a minimum $p_{\mathrm{T}}^{\mathrm{jet}}$ of 100 GeV for anti-k_t $R = 0.4$ jets. The jet trigger was fully efficient for the $p_{\mathrm{T}}^{\mathrm{jet}}$ range considered in this measurement.

3 Data Samples and Event Selection

The data used in this analysis is taken from the 2018 Pb+Pb and 2017 pp runs, both at $\sqrt{s_{\mathrm{NN}}} = 5.02$ TeV. The average number of collisions per bunch-crossing (pile-up) was 0.003 in the Pb+Pb data and ranges from 1.4 to 4.4 in the pp data depending on the data-taking run. Events in both Pb+Pb and pp collisions were collected using the jet triggers with the same p_{T} threshold as described above. The events are required to have been collected during stable beam conditions, and to satisfy detector and data-quality requirements [46]. Both pp and Pb+Pb events are required to have at least one reconstructed primary vertex, and the Pb+Pb events are further required to satisfy nominal offline minimum-bias Pb+Pb collision criteria, identical to those used in Ref. [47]. This additional requirement identifies and rejects 0.2% of the selected events as pile-up events, based on a combination of the total transverse energy E_{T} measured in the FCal, denoted by $\Sigma E_{\mathrm{T}}^{\mathrm{FCal}}$, and the total energy deposited in the ZDC.

The degree of geometric overlap of the colliding Pb+Pb nuclei is characterized by event centrality. The procedure used to experimentally define centrality classes in this note follows that used in other measurements of Pb+Pb collisions performed by the ATLAS Collaboration [26]. The distribution of total transverse energy deposits in the FCal is divided into successive quantiles of the total inelastic cross-section for Pb+Pb collisions, with the largest $\Sigma E_{\mathrm{T}}^{\mathrm{FCal}}$ events corresponding, on average, to the events with the largest geometric overlap between the colliding nuclei. The centrality intervals used are: 0–10% (largest $\Sigma E_{\mathrm{T}}^{\mathrm{FCal}}$), 10–30%, 30–50%, and 50–80%. A Glauber model analysis of $\Sigma E_{\mathrm{T}}^{\mathrm{FCal}}$ distribution is used to evaluate the mean nuclear thickness function, $\langle T_{\mathrm{AA}} \rangle$, for different centrality intervals [48, 49]. The $\langle T_{\mathrm{AA}} \rangle$ values and uncertainties, which are discussed in Ref. [50], are listed in Table 1 for each centrality selection considered in this measurement.

The Monte Carlo (MC) simulations used in this analysis are multijet events generated with the Pythia8 [51] MC generator with leading-order matrix elements for dijet production which were matched to the parton shower. The A14 set of tuned parameters [52] and the NNPDF23lo parton distribution functions [52] are used. For Pb+Pb collisions the simulated Pythia8 MC generator dijet events are overlaid with

Centrality selection	$\langle T_{\mathrm{AA}} \rangle \pm \delta \langle T_{\mathrm{AA}} \rangle$ [1/mb]
0–10%	23.21 ± 0.06
10–30%	11.57 ± 0.12
30–50%	3.92 ± 0.11
50–80%	0.73 ± 0.04

Table 1: The $\langle T_{\mathrm{AA}} \rangle$ values and uncertainties for the centrality selections used in this measurement.

minimum-bias Pb+Pb data, and this "overlay" sample is reweighted on an event-by-event basis to obtain the same centrality distribution as the jet-triggered Pb+Pb data sample. For each event, the PYTHIA8 generation and subsequent GEANT4 [53] simulations reproduce the detector conditions in the data-taking run. This allows for the simulations to account for underlying event (UE) effects in the jet reconstruction. The simulations are digitized and reconstructed in the same way as the data.

4 Analysis Procedure

4.1 Jet Reconstruction

The jet reconstruction procedures follow those used by the ATLAS Collaboration for previous jet measurements in Pb+Pb collisions [23, 54]. Jets are reconstructed using the anti-k_t algorithm [40] implemented in the `FastJet` software package [55]. In both pp and Pb+Pb collisions, jets with $R = 0.4$ are formed by clustering calorimeter towers of spatial size $\Delta\eta \times \Delta\phi = 0.1 \times \pi/32$ in the pseudorapidity range $|\eta| < 4.9$ over the full azimuthal range. The energies in the towers are obtained by summing the energies of calorimeter cells at the electromagnetic energy-scale [56] within the tower boundaries. The UE contribution to each tower is subtracted on an event-by-event basis by estimating the average local energy density, $\rho(\eta, \phi)$. This estimate is obtained by measuring the average energy in calorimeter towers as a function of η and including the azimuthal modulation due to harmonic flow characterized by the second-, third-, and fourth-order flow coefficients [57]. An iterative procedure is applied to remove potential biases from the jets in the determination of ρ [54]. Following the UE subtraction, new estimates of ρ are obtained by excluding the contributions of towers in jets from the average energy density and flow parameterization. Additionally, the UE is also corrected for η- and ϕ-dependent non-uniformities of the detector response to soft particles by correction factors derived in minimum-bias Pb+Pb data. In pp collisions, the same background subtraction procedure is applied, but without this non-uniformity correction and assuming no harmonic modulation of the UE.

Following the UE subtraction, η- and p_{T}-dependent multiplicative calibration factors derived in MC simulations are applied to the jet four-momentum vector to account for the non-compensating hadronic response of the calorimeter [58]. An additional correction based on in situ studies of jets recoiling against photons, Z bosons, and jets in other regions of the calorimeter is applied to account for known differences between data and the MC sample used to derive the calibration [26]. This calibration is followed by a cross-calibration which relates the jet energy-scale (JES) of jets reconstructed by the procedure outlined in this section to the JES in 13 TeV pp collisions [58]. The performance of the jet reconstruction in pp and Pb+Pb collisions has been studied in detail in Ref. [23]. The jet transverse momentum, referred to as $p_{\mathrm{T}}^{\mathrm{jet}}$, is defined as the calibrated p_{T} of $R = 0.4$ jets formed from calorimeter towers. Calibrations are applied to the p_{T} of the jet and not individually to the constituent calorimeter towers in this procedure. Fully calibrated

jets having $p_{\mathrm{T}}^{\mathrm{jet}}$ above 158 GeV and $|\eta| < 2.1$ are used in this measurement. The $p_{\mathrm{T}}^{\mathrm{jet}}$ threshold of 158 GeV has been chosen to allow for direct comparisons with earlier studies[23]. Truth-level jets are defined in the MC events by applying the anti-k_t algorithm with $R = 0.4$ to stable particles with a proper lifetime greater than 30 ps, but excluding muons and neutrinos, which do not leave significant energy deposits in the calorimeter.

4.2 Jet Constituents

The granularity of the ATLAS calorimeter towers, which are used as constituents in the initial jet reconstruction, lacks the angular resolution to resolve collimated prongs of a jet with small opening angles comparable to the expected resolving power of the QGP [38, 39]. In order to improve the angular and energy resolution of the jet constituents, new constituents are defined by combining the superior angular resolution of the tracker with calorimeter information. These objects, referred to as track-calo-clusters (TCCs), are built using the energies of topological cell clusters (topo-clusters) [59] and the spatial coordinates of charged tracks [60]. TCCs have been used in previous ATLAS studies to improve the resolution of jet substructure variables used in W/Z-boson tagging [61]. They are also used in combination with particle-flow [62] objects to optimize jet reconstruction in pp collisions [63]. In this measurement, TCCs are reconstructed in a manner similar to that in Ref. [60] but with some modifications to account for the UE in Pb+Pb collisions as detailed below.

Topo-clusters, used to define the energy-scale of the TCCs, are built from calorimeter cells using a noise-suppression algorithm [59] and have been used extensively in jet substructure measurements in pp collisions [10, 11]. In Pb+Pb collisions, a ϕ-modulated background subtraction, similar to the UE subtraction procedure employed for jet reconstruction (Section 4.1), is applied to the calorimeter cells before using them to build topo-clusters. Charged-particle tracks are reconstructed from hits in the inner detector using standard optimization algorithms for Pb+Pb collisions as detailed in Refs. [64, 65]. Reconstructed tracks used in the TCC reconstruction as seeds are required to have $p_{\mathrm{T}} > 3$ GeV and also meet several criteria intended to select primary charged particles [29]. Tracks in an event are extrapolated to the calorimeter and are matched to a single or multiple topo-clusters based on the topo-cluster size and the track extrapolation uncertainty.

Following the track and topo-cluster matching, the procedure to determine TCC four-momentum vectors is described briefly below and is detailed further in Ref. [60]. For an isolated match between a track from the selected primary vertex and a topo-cluster, the topo-cluster energy and the track direction are used to form a single TCC. In the case of topo-clusters which do not match any tracks, the topo-cluster's four-momentum vector is directly used to create a TCC. Conversely, instances where tracks are not matched to any topo-clusters, observed to occur in less than 1% of the cases, are treated analogously by creating a TCC using the track's four-momentum vector. In cases where multiple tracks are matched to one or multiple topo-clusters, the TCC algorithm is designed to create exactly one TCC object per track originating from the primary vertex. Such multiple matches are handled by using the track's angular coordinates, while splitting the topo-cluster energy between the corresponding TCC objects to account for energy sharing between the different matches.

The topo-cluster energy sharing procedure in the TCC reconstruction for tracks matched to clusters makes use of three general concepts and has been detailed in Ref. [60]. First, each cluster matched to the seed track should contribute to the resulting TCC object proportionally to its p_{T} fraction out of all matched clusters. Second, each cluster could be matched to multiple TCC objects, so its contribution to a given

TCC is weighted by the fraction of p_{T} designated for the seed track compared to all other tracks matched to the cluster. Third, the proportion of topo-cluster energy demanded by each of those tracks is itself weighted by the fraction of energy that the cluster represents compared to all other clusters matching the track. The 3 GeV p_{T} threshold on the charged tracks in the TCC reconstruction has been optimized to avoid low-p_{T} UE tracks sharing energy of high-p_{T} topo-clusters.

All TCCs having $p_{\mathrm{T}} > 4$ GeV are used in this measurement. Jets considered in this measurement with $p_{\mathrm{T}}^{\mathrm{jet}} > 158$ GeV and $|y| < 2.1$ have an average of $6-7$ TCCs above the 4 GeV threshold associated with the jet in pp and Pb+Pb collisions. TCCs built by matching tracks to topo-clusters account for ~77% (~59%) of the total number of TCCs within a jet in pp (central Pb+Pb) collisions. The remaining TCCs are predominantly cases where topo-clusters are not matched to any tracks.

4.3 Jet Grooming and r_{g}

Jet grooming algorithms are used to isolate prongs of a jet that correspond to a hard splitting in the parton shower evolution by systematically removing the contribution of soft wide-angle radiation. The soft-drop grooming procedure [9], a generalization of the modified mass-drop tagger [8] is employed in this measurement to single out perturbative radiation from soft, mostly non-perturbative components of the jet [15–17, 33]. The angular distance between the subjets selected to tag the first hard splitting of a jet, r_{g}, is measured in this analysis.

The procedure starts with re-clustering the constituents of a jet using the Cambridge-Aachen (C/A) algorithm [66, 67] to form a clustering tree with a purely angular-ordered structure. In this measurement, jets are initially reconstructed using calorimeter towers with the anti-k_t algorithm as described in Sec. 4.1, and their response is well-defined [54]. Calorimeter tower jets satisfying the kinematic thresholds listed in Sec. 4.1 are selected to be re-clustered using the TCCs associated with the jet. TCCs having p_{T} above 4 GeV, and within $\Delta R < 0.4$ from a reconstructed jet axis are utilized in the jet re-clustering process of the soft-drop procedure. The 4 GeV threshold on the TCCs, applied only at the detector-level, is used to minimize UE effects on precisely measuring r_{g}. At the truth-level in MC events, all stable charged and neutral particles within the truth jets are used in the soft-drop re-clustering procedure. The C/A algorithm clusters the nearest constituents first, working outwards towards the wider constituents, independent of their p_{T}. The C/A re-clustered jet is then recursively declustered into two "subjets" and is determined if the subjets sj_1 and sj_2 with transverse momenta $p_{\mathrm{T}}^{sj_1}$ and $p_{\mathrm{T}}^{sj_2}$ satisfy the soft-drop condition:

$$\frac{\min(p_{\mathrm{T}}^{sj_1}, p_{\mathrm{T}}^{sj_2})}{p_{\mathrm{T}}^{sj_1} + p_{\mathrm{T}}^{sj_2}} > z_{\mathrm{cut}} \left(\frac{\Delta R_{12}}{R}\right)^{\beta}, \tag{1}$$

where z_{cut} and β are algorithm parameters, R is the radius used to cluster the jets ($R = 0.4$), and $\Delta R_{12} = \sqrt{\Delta\eta_{12}^2 + \Delta\phi_{12}^2}$ is the distance in $\eta - \phi$ between the subjets. If the soft-drop condition in Eq. 1 is not satisfied, then the subjet with the smaller p_{T} is dropped and the procedure is then iterated on the remaining subjets. If the soft-drop condition is satisfied at any point, the algorithm terminates and r_{g} is set to be the ΔR_{12} between the subjets sj_1 and sj_2.

If the condition described in Eq. 1 is never satisfied, $r_{\mathrm{g}} = 0$ is assigned to the jet to indicate that the soft-drop procedure cannot find two subjets that satisfy Equation 1. Jets with $r_{\mathrm{g}} = 0$ are primarily those with a single TCC object or truth particle carrying a significant fraction of the jet energy. For all $z_{\mathrm{cut}} > 0$ and $\beta > 0$, the procedure is infrared- and collinear-safe, while it is infrared-safe when $\beta = 0$ [9]. The

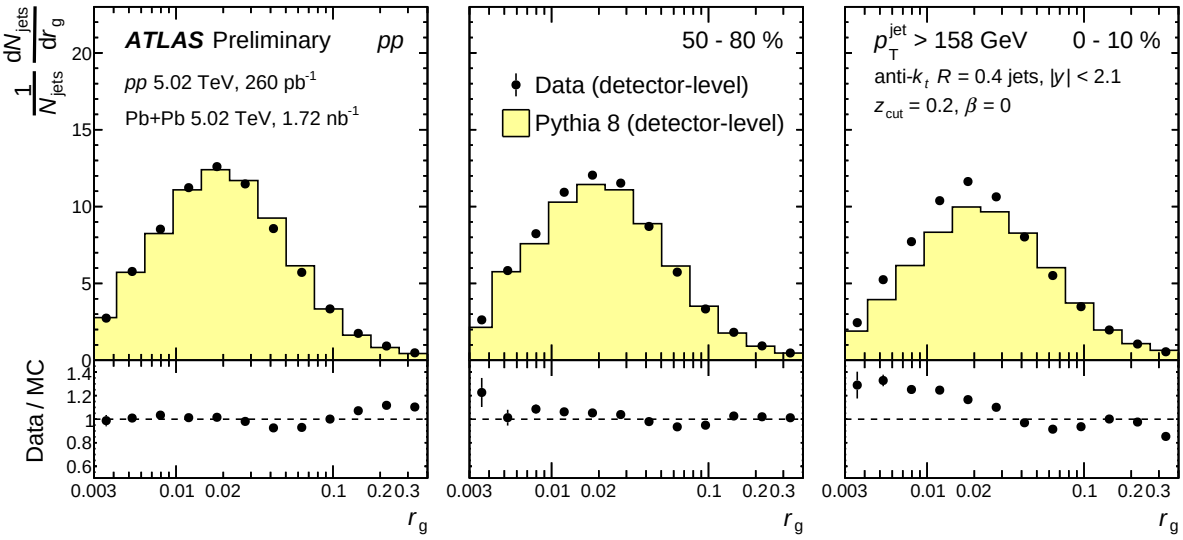

Figure 1: Top: Self-normalized r_g distributions measured using TCCs at the detector-level from pp at $\sqrt{s}$ = 5.02 TeV (left) and Pb+Pb data $\sqrt{s_{NN}}$ = 5.02 TeV (second and third panels) for different centrality bins, compared to the detector-level distributions predicted by the Pythia 8 generator. The error bars represent statistical uncertainties. Bottom: Ratios of r_g distributions at the detector-level in data to MC. The legend applies to all the panels.

soft-drop parameters $z_{cut} = 0.2$ and $\beta = 0$, corresponding to an angle-independent grooming setting, are used for the results shown. These parameters are chosen to optimize the purity of selecting the two hardest prongs of the jet against the competing effect of jets failing the soft-drop grooming with a high z_{cut} value. At the truth-level, less than 4% of the total jets fail the soft-drop condition using parameters $z_{cut} = 0.2$ and $\beta = 0$, thereby minimizing the possible bias of looking at different populations of jets in pp and Pb+Pb collisions. The r_g of a jet measured using $z_{cut} = 0.2$ and $\beta = 0$ is also observed to be insensitive to lowering the 4 GeV threshold on the TCCs.

Distributions of r_g measured using TCCs at the detector-level from pp and Pb+Pb data are shown in Figure 1, and are compared to the detector-level distributions from the Pythia 8 MC events. The detector-level r_g distributions measured using TCCs show good agreement between data and MC in pp and peripheral Pb+Pb collisions. The difference in r_g distributions between data and MC in central Pb+Pb collisions arises from quenching effects, not modeled in MC, and is discussed in detail in the results section (Section 6). No systematic uncertainties are shown for this plot as it is only intended to demonstrate the performance of TCCs in measuring r_g.

4.4 Unfolding

The jet yields are unfolded in both jet p_T^{jet} and r_g in order to account for non-uniformities in detector performance and bin migration due to the finite resolutions of jet energy, TCC energy, and TCC position, including migration in and out of the measurement phase space. The measurement phase space in this analysis corresponds to $p_T^{jet} > 158$ GeV, $|\eta| < 2.1$, and $0 < r_g < 0.4$ for the jets.

At the truth level, the soft-drop procedure is applied to truth jets using all stable charged and neutral particles within the jet as constituents. Utilizing the RooUnfold package [68], the yields of groomed

jets are unfolded using a two-dimensional Bayesian iterative unfolding algorithm [69] simultaneously in $p_{\mathrm{T}}^{\mathrm{jet}}$ and r_{g}, while the inclusive jet yields are unfolded using a one-dimensional unfolding in $p_{\mathrm{T}}^{\mathrm{jet}}$. The migration matrices are reweighted simultaneously in truth $p_{\mathrm{T}}^{\mathrm{jet}}$ and r_{g} by the ratios of the corresponding distributions in data to those in the reconstructed MC sample, separately for pp and each centrality class in Pb+Pb collisions. The uncertainty from the reweighting procedure is estimated by unfolding with and without the reweighting factors and are detailed in Section 5. The effects of inefficiencies and misidentified jets in the measurement are accounted for in the analysis by applying an efficiency correction and subtraction procedure, respectively, through the unfolding procedure. In the iterative Bayes unfolding method implemented in RooUnfold, the inefficiencies are handled by applying a multiplicative factor to each truth bin of the migration matrix. The inefficiencies in this measurement arise predominantly from jets migrating out of the measurement phase space at the detector-level due to energy resolution effects and from jets that fail the soft-drop grooming procedure. Truth-level jets having significantly lower p_{T} than 158 GeV ($p_{\mathrm{T}}^{\mathrm{jet}}$ threshold) that migrate into the measurement phase space at the detector-level are treated as misidentified jets. The rate of such misidentified jets is observed to be negligible in this measurement, and are accounted for by treating them as an additive background. The effect of jets reconstructed entirely from overlapping UE particles in this measurement is insignificant.

The migration matrices used in the unfolding procedure are binned uniformly on logarithmic scales and have 13 bins along r_{g} from 0 to 0.4 and 16 bins along $p_{\mathrm{T}}^{\mathrm{jet}}$ from 158 GeV to 1 TeV. Additionally, in the truth phase space, $p_{\mathrm{T}}^{\mathrm{jet}}$ has one overflow and six underflow bins down to 80 GeV for a smooth inefficiency correction, and r_{g} has one overflow and one underflow bin in the migration matrix. There is no significant migration across centrality bins in this measurement. A separate migration matrix is generated for each centrality bin in Pb+Pb collisions using the Pythia8 sample overlaid with minimum-bias Pb+Pb data and for pp collisions using the Pythia8 sample. The number of iterations in the unfolding procedure is optimized independently for different centrality intervals to balance unfolding closure and fluctuations in MC samples. The optimal number of iterations are set to be 4-6 depending on the centrality bin. The unfolding closure evaluated in MC samples is better than 1%.

The differential jet cross-section in pp collisions is defined as:

$$\frac{\mathrm{d}^2\sigma_{\mathrm{jet}}}{dp_{\mathrm{T}}^{\mathrm{jet}}dr_{\mathrm{g}}} = \frac{1}{L_{\mathrm{int}}}\frac{N_{\mathrm{jets}}}{\Delta p_{\mathrm{T}}^{\mathrm{jet}}\Delta r_{\mathrm{g}}}, \tag{2}$$

where N_{jets} is the unfolded jet yield, Δp_{T} and Δr_{g} are the widths of the p_{T} and r_{g} bins and L_{int} is the integrated luminosity.

The per minimum-bias event jet yield in Pb+Pb collisions, referred to as per-event yield for simplicity, is defined as:

$$\frac{1}{N_{\mathrm{evt}}^{\mathrm{cent}}}\frac{\mathrm{d}^2N_{\mathrm{jet}}^{\mathrm{cent}}}{dp_{\mathrm{T}}^{\mathrm{jet}}dr_{\mathrm{g}}} = \frac{1}{N_{\mathrm{evt}}^{\mathrm{cent}}}\frac{N_{\mathrm{jets}}^{\mathrm{cent}}}{\Delta p_{\mathrm{T}}^{\mathrm{jet}}\Delta r_{\mathrm{g}}}, \tag{3}$$

where $N_{\mathrm{jet}}^{\mathrm{cent}}$ is the unfolded jet yield in Pb+Pb collisions within a certain $p_{\mathrm{T}}^{\mathrm{jet}}$ and r_{g} interval for a given centrality (denoted by the superscript "cent"), and $N_{\mathrm{evt}}^{\mathrm{cent}}$ is the the number of minimum-bias events in the centrality class.

Modification of the jet yield in Pb+Pb collisions in a given centrality interval compared to that in pp collisions is quantified using the nuclear modification factor, R_{AA}, defined as:

$$R_{\mathrm{AA}}(p_{\mathrm{T}}^{\mathrm{jet}}, r_{\mathrm{g}}) = \frac{1}{N_{\mathrm{evt}}^{\mathrm{cent}}} \frac{1}{\langle T_{\mathrm{AA}} \rangle} \frac{\frac{\mathrm{d}^2 N_{\mathrm{jet}}^{\mathrm{cent}}}{dp_{\mathrm{T}}^{\mathrm{jet}} dr_{\mathrm{g}}}}{\frac{\mathrm{d}^2 \sigma_{\mathrm{jet}}}{dp_{\mathrm{T}}^{\mathrm{jet}} dr_{\mathrm{g}}}}, \tag{4}$$

where $\langle T_{\mathrm{AA}} \rangle$ is the average nuclear thickness function, presented in Table 1. At a given $p_{\mathrm{T}}^{\mathrm{jet}}$, r_{g}, and centrality interval, $R_{\mathrm{AA}} < 1$ indicates a suppression in jet production in Pb+Pb collisions compared to that in pp collisions.

5 Systematic Uncertainties

Several sources of systematic uncertainties are considered for this analysis. The systematic uncertainties on the jet cross-sections in pp and per-event yields in Pb+Pb collisions arise from the jet energy-scale and resolution, the constituent TCC energy-scale and resolution, the unfolding procedure, integrated luminosity (pp only), and $\langle T_{\mathrm{AA}} \rangle$ (Pb+Pb only).

The systematic uncertainty on the JES has three parts. The first (labeled 'JES baseline' in Figures 2-5) is a centrality-independent component that is determined from in situ studies of the calorimeter response to jets reconstructed with the procedure used in 13 TeV pp collisions [56, 70], with an additional component which accounts for the relative energy-scale difference between the jet reconstruction procedures used in 13 TeVpp collisions and in this measurement [58]. The potential mis-modeling of relative abundances of jets initiated by quarks and gluons in the MC and of the calorimetric response to quark and gluon jets, are accounted for by the second component (labeled 'JES flavor' in Figures 2-5). The third, centrality-dependent component (applicable in Pb+Pb collisions only and labeled 'JES quenching' in Figures 2-5) accounts for modifications of the parton shower due to quenching [29] resulting in a different detector response to jets in Pb+Pb collisions that is not modeled by the MC simulation. It is evaluated by the method used for 2011 and 2015 data [58], which compares the jet p_{T} measured in the calorimeter and the sum of p_{T} of charged particles within the jet, in both the data and MC samples. The charged-particle tracks are selected with $p_{\mathrm{T}} > 4$ GeV to exclude particles from the UE. The ratio of the sum of the charged-particle p_{T} to the $p_{\mathrm{T}}^{\mathrm{jet}}$ provides a data-driven estimate of the centrality dependence of the JES. The centrality-dependent JES is the dominant source of uncertainty on the jet R_{AA} measurement contributing to a relative uncertainty of ~8% in central collisions.

The uncertainty due to the jet energy resolution (JER) is evaluated by applying a Gaussian smearing factor to the reconstructed $p_{\mathrm{T}}^{\mathrm{jet}}$ in the MC sample. The smearing factor is evaluated using an in situ technique in 13 TeV pp data that involves studies of dijet p_{T} balance [70, 71]. Further, an uncertainty is included to account for differences between the tower-based jet reconstruction and the jet reconstruction used in 13 TeV pp data analyses, as well as differences in calibration procedures [58]. The jet-related uncertainties are evaluated in the analysis by modifying the migration matrix for each uncertainty contribution. The modifications from the nominal unfolded result for each variation are then combined in quadrature to calculate the total JES and JER contribution. The jet energy-scale and resolution are the dominant sources of uncertainty in measuring the jet cross-sections and R_{AA} in this analysis and contribute to a maximum relative uncertainty of about 14% and 9%, respectively.

The TCC energy response is primarily determined by the topo-cluster energy response. The uncertainties on topo-cluster energy-scale and resolution, measured using 13 TeV pp data [11], are directly applied to

pp data. The cluster uncertainties from 13 TeV pp data [11] are scaled conservatively by a factor of 2 for Pb+Pb data to cover the uncertainty in the topo-cluster energy response in the dense Pb+Pb collision environment. The inefficiency of matching between track and topo-cluster is driven by the topo-cluster angular resolution. A random Gaussian smearing of 5 mrad is independently applied in η and ϕ following previous ATLAS measurements [11, 72] to account for potential mis-modeling of topo-cluster positions and are observed to have a negligible effect on the resulting TCCs and the r_{g} distributions. TCCs are reconstructed using the varied topo-cluster energies and positions according to their uncertainties in MC events and are used to unfold the nominal data and propagated through the full analysis procedure. The modifications from the nominal unfolded result for each of the topo-cluster uncertainty source is then combined in quadrature.

The effects of topo-cluster splitting and merging have been studied in detail following previous measurements [11]. The MC generator predictions are observed to precisely describe each of the splitting and merging scenarios tested in data and thus there is no significant systematic uncertainty associated with this procedure.

The angular coordinates (η, ϕ) of a TCC corresponding to a charged particle is determined by the track seeding the TCC object. Systematic variations of these coordinates are evaluated to account for tracking mis-modeling in MC events. These differences are decomposed into two components: one from the uncertainty in the inner detector material derived in pp collisions [73], and a second from the modeling of pixel cluster merging inside dense environments [64, 74], such as inside the core of high-energy jets and in central Pb+Pb collisions. These track uncertainties are propagated through the TCC reconstruction and are observed to have a negligible effect on the final r_{g} distributions.

The TCC energy uncertainties typically have a modest effect on this measurement compared to jet-related uncertainties as only the angular distance between the subjets (r_{g}) is measured. They become significant with a relative uncertainty up to 15% at large r_{g} (>0.3) in central Pb+Pb collisions as UE fluctuations in the outer region of the jet lead to a deteriorated performance in identifying the hard subjets.

The differences between the unfolded results with and without the migration matrix reweighting factors are assigned as systematic uncertainties arising from the unfolding procedure. The unfolding uncertainty is observed to have a smaller effect compared to other sources, contributing to a relative uncertainty of <5% on the cross-section, yield, and R_{AA} results.

The statistical uncertainties in the unfolding due to statistical errors on the data were evaluated using the pseudo-experiment technique with 500 separate stochastic variations of the input spectrum as described in Ref. [68]. The contributions of statistical fluctuations in the response matrix were similarly evaluated using an equal number of stochastic variations. The two contributions to the statistical uncertainty were combined in quadrature and are observed to have a contribution <1% to the total systematic uncertainties on the results.

In the 2017 pp data, the LUCID-2 detector [75] was used for the primary luminosity measurement. The uncertainty on the integrated luminosity is derived using the methods described in Ref. [76] and is estimated to be 1.6%. For Pb+Pb collisions, the systematic uncertainty on the mean nuclear thickness function, $\langle T_{\mathrm{AA}} \rangle$, is estimated by varying the MC Glauber model parameters as detailed in Ref. [57], and is listed in Table 1.

A summary of the relative uncertainties on the unfolded inclusive jet cross-sections, yields, and nuclear modification factor are shown in Figures 2 through 5.

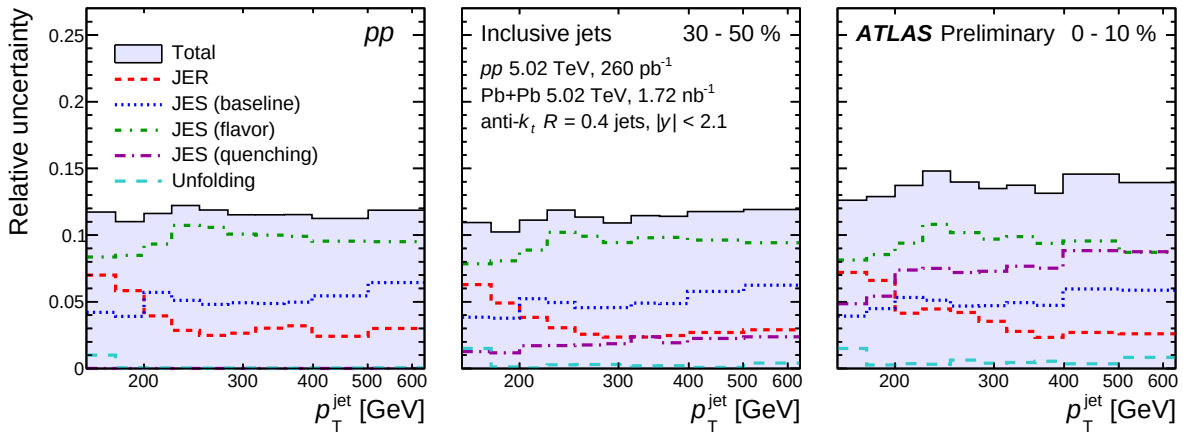

Figure 2: The relative systematic uncertainties on inclusive $p_{\mathrm{T}}^{\mathrm{jet}}$ cross-section and per-event jet yield measurements in pp collisions at $\sqrt{s}$ = 5.02 TeV (left) and for different event centralities in Pb+Pb collisions at $\sqrt{s_{\mathrm{NN}}}$ = 5.02 TeV (second and third panels). The legend applies to all the panels.

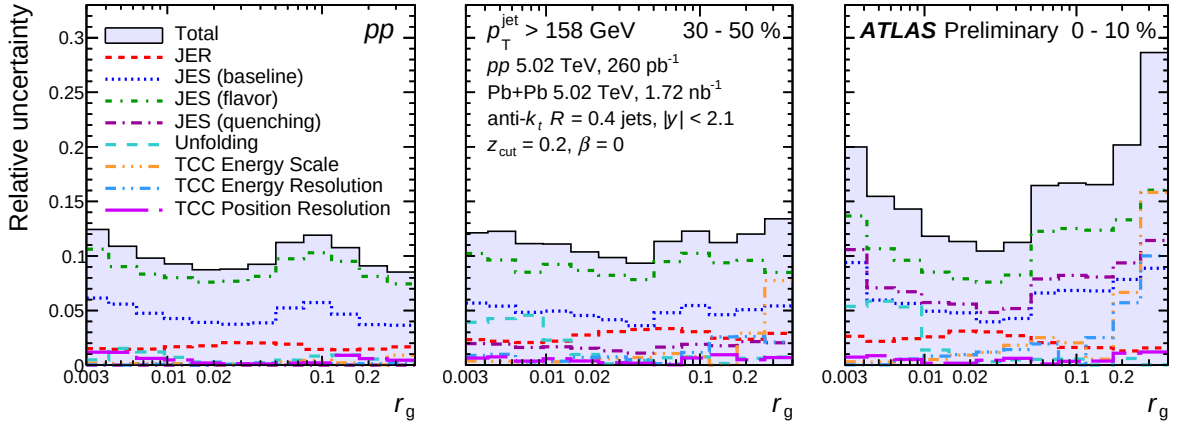

Figure 3: The relative systematic uncertainties on inclusive r_{g} cross-section and per-event jet yield measurements in pp collisions at $\sqrt{s}$ = 5.02 TeV (left) and for different event centralities in Pb+Pb collisions at $\sqrt{s_{\mathrm{NN}}}$ = 5.02 TeV (second and third panels) shown for soft-drop parameters $z_{\mathrm{cut}} = 0.2$ and $\beta = 0$. The legend applies to all the panels.

Figures 2 and 3 present a summary of the total and individual relative uncertainties on the jet cross-sections and per-event yields as a function of $p_{\mathrm{T}}^{\mathrm{jet}}$ and r_{g}, respectively. All of the uncertainties are summed in quadrature to obtain the total uncertainty. The jet energy-scale is the dominant source of uncertainty on the cross-sections and per event jet yields except for large r_{g} regions in central Pb+Pb collisions, where the TCC energy-scale uncertainties also have a comparable effect. A summary of the total and individual relative uncertainties on the nuclear modification factor, R_{AA}, are shown in Figures 4 and 5 as a function of $p_{\mathrm{T}}^{\mathrm{jet}}$ and r_{g}, respectively. The uncertainties which are common between pp and Pb+Pb collisions, such as the centrality-independent JES and JER uncertainties, are treated as correlated when determining the uncertainty on the R_{AA}. However, as the centrality-dependent component of the JES uncertainty (only for Pb+Pb collisions) do not cancel out in the cross-section ratios, they become the dominant source of uncertainty in the R_{AA} results.

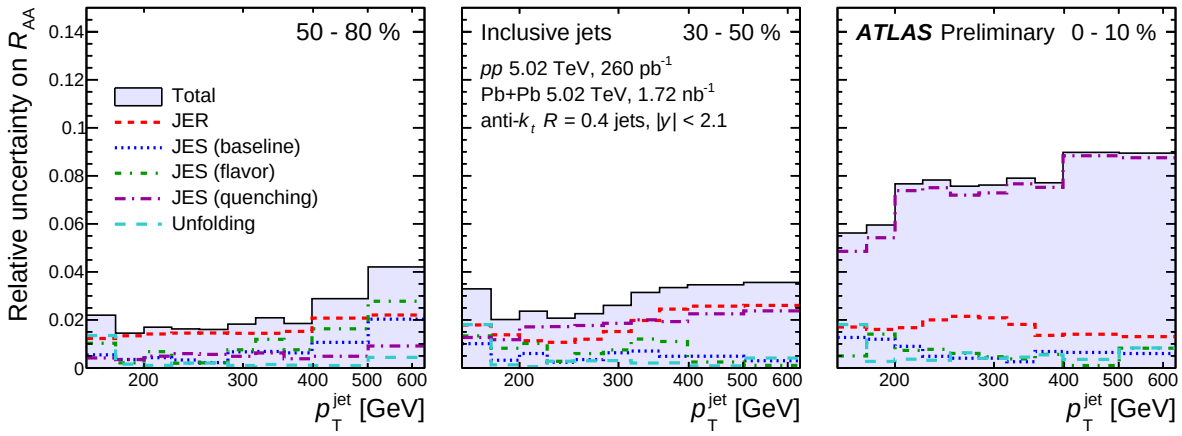

Figure 4: The relative systematic uncertainties on the R_{AA} measurements as a function of p_T^{jet} in different centrality intervals of Pb+Pb collisions at $\sqrt{s_{NN}}$ = 5.02 TeV. The legend applies to all the panels.

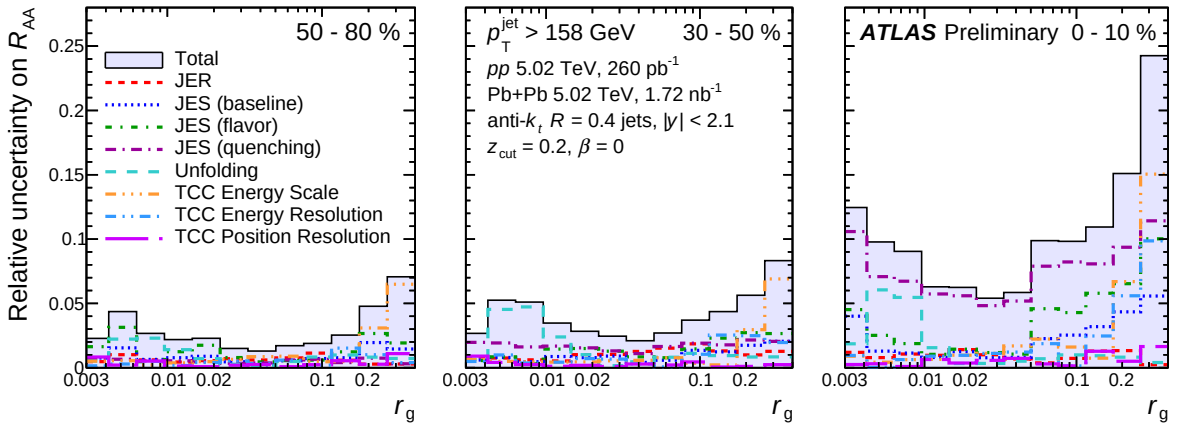

Figure 5: The relative systematic uncertainties on the R_{AA} measurements as a function of r_g in different centrality intervals of Pb+Pb collisions at $\sqrt{s_{NN}}$ = 5.02 TeV shown for soft-drop parameters z_{cut} = 0.2 and β = 0. The legend applies to all the panels.

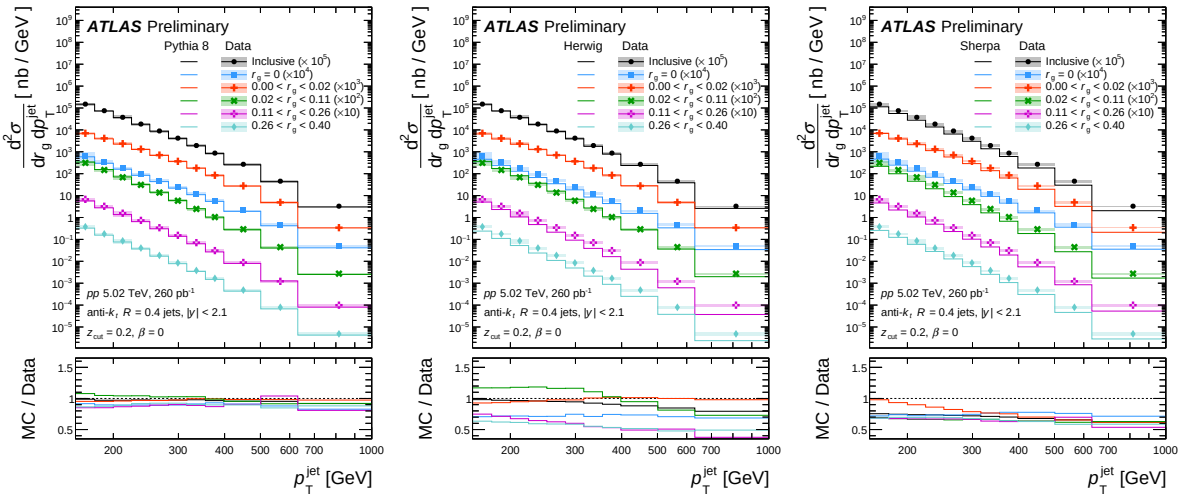

Figure 6: Differential cross-section of jets passing the soft-drop grooming condition in different r_g intervals in pp collisions at $\sqrt{s}$ = 5.02 TeV as a function of p_T^{jet}. Distributions for inclusive jets (no grooming) and for those jets that fail the soft-drop requirement (r_g =0) are also shown. The single differential cross section for inclusive jets (no grooming) is also shown. For each r_g interval from large r_g to small r_g and inclusive (no grooming), an additional scaling factor of 10 is applied to the plotted points for visual clarity. The pp jet cross-sections are compared to predictions from three MC generators, Pythia 8 (left), Herwig (middle) and Sherpa (right). The error bars represent statistical uncertainties, and shaded bars represent systematic uncertainties. The global uncertainty on the pp luminosity of 1.6% is not shown. The ratios of jet cross-section predictions from different MC generators to the unfolded data are shown in the lower panels. No systematic uncertainty is shown in these ratios.

6 Results

The unfolded differential jet cross-sections obtained from pp collision data are shown in Figure 6 as a function of p_T^{jet} and r_g. The differential cross-sections are reported for four bins in r_g, each scaled up by successive powers of 10. The cross-section is also reported for jets that fail the soft-drop grooming condition. These are referred to as $r_g = 0$ in this analysis and they make up about 3.5% of the inclusive pp jet cross-section.

Figure 7 shows the unfolded inclusive differential cross-section in pp collision data as a function of r_g. The differential cross-sections in r_g are also reported for four bins in p_T^{jet}. The distributions are observed to peak at lower values of r_g with increasing p_T^{jet}. The collimation of jets with increasing p_T^{jet} is expected from the larger boost of the fragmenting parton and an increased quark-initiated jet fraction [60].

The jet differential cross-sections measured in pp data are compared to truth-level predictions by the Pythia, Herwig, and Sherpa generators in Figures 6 and 7. The Herwig predictions are obtained from multijet events at next-to-leading order generated by Herwig 7.1.3 generator [77] with NNPDF3.0 PDF set [78] for the matrix element calculation. The Sherpa predictions are from multijet events generated using the Sherpa 2.2.5 [79] generator with default Sherpa parton shower [80] based on Catani–Seymour dipole factorisation and the NNPDF3.0 PDF set [78]. The Pythia predictions are observed to describe the data well in inclusive and differential bins of p_T^{jet} and r_g. The Herwig and Sherpa predictions underestimate the cross-sections but describe the shape of the inclusive jet differential cross-section as a function of p_T^{jet} as well as the differential cross-section in different r_g bins. The Herwig generator predicts a slightly

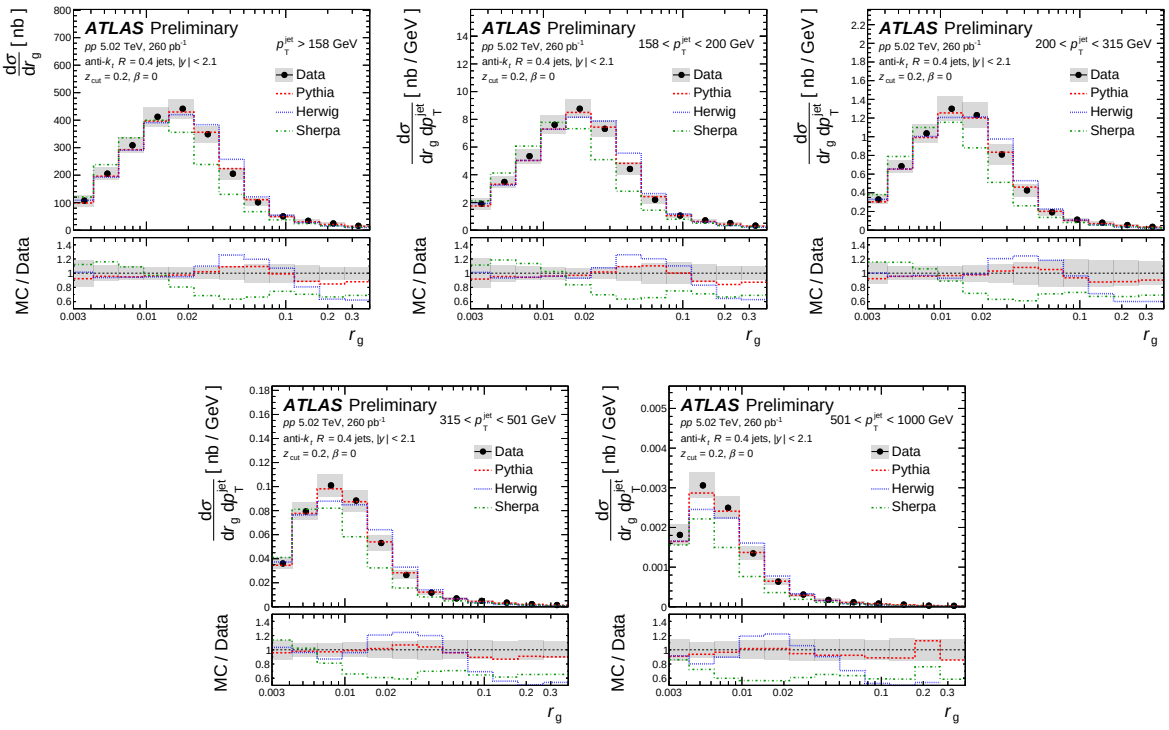

Figure 7: Differential cross-section of jets passing soft-drop grooming condition in pp collisions at $\sqrt{s} = 5.02$ TeV as a function of r_{g} is shown for different $p_{\mathrm{T}}^{\mathrm{jet}}$ intervals and also for $p_{\mathrm{T}}^{\mathrm{jet}} > 158$ GeV. The error bars represent statistical uncertainties, shaded bars represent systematic uncertainties. The global uncertainty on the pp luminosity of 1.6% is not shown. The ratios of jet cross-section predictions from different MC generators to the unfolded data are shown below. The shaded bars in the bottom panels represent systematic uncertainties on inclusive cross-section ratios.

wider r_{g} distributions compared to pp data across all $p_{\mathrm{T}}^{\mathrm{jet}}$ regions studied here. The SHERPA generator predicts a significantly narrower r_{g} distribution compared to pp data at low $p_{\mathrm{T}}^{\mathrm{jet}}$ and underestimates the jet cross-sections at high $p_{\mathrm{T}}^{\mathrm{jet}}$. The trend of collimation of jets with increasing $p_{\mathrm{T}}^{\mathrm{jet}}$ observed in pp data is reproduced by all three MC generators with varying levels of accuracy.

Figures 8 and 9 show the Pb+Pb per-event yields normalized by $\langle T_{\mathrm{AA}} \rangle$ for four centrality intervals as a function of $p_{\mathrm{T}}^{\mathrm{jet}}$ and r_{g}, respectively. The yields are also shown for jets that fail the soft-drop grooming condition ($r_g = 0$) as a function of the $p_{\mathrm{T}}^{\mathrm{jet}}$, and account for about 4–5.5% of the inclusive Pb+Pb jet yield. The per-event jet yields in Pb+Pb data normalized by the $\langle T_{\mathrm{AA}} \rangle$ fall below the corresponding pp jet cross-sections for a given r_{g} or $p_{\mathrm{T}}^{\mathrm{jet}}$ interval, indicating jet suppression, and this difference increases with increasing centrality and r_{g}. The r_{g} distributions are also observed to peak at lower values of r_{g} with increasing $p_{\mathrm{T}}^{\mathrm{jet}}$ in both pp and all centrality bins in Pb+Pb collisions. The jet $p_{\mathrm{T}}^{\mathrm{jet}}$ spectra are observed to have relatively similar slopes in the different r_{g} regions for both pp and Pb+Pb collisions.

The nuclear modification factor, R_{AA}, which quantifies the jet suppression in Pb+Pb collisions compared to pp, is shown as a function of $p_{\mathrm{T}}^{\mathrm{jet}}$ in Figure 10 and as a function of r_{g} in Figure 11 for four centrality intervals. The R_{AA} for inclusive jets is observed to vary from ~0.95 for jets in the 50 − 80% centrality bin to ~0.55 for the most central collisions. The R_{AA} for inclusive jets is also observed to have an upward slope with increasing $p_{\mathrm{T}}^{\mathrm{jet}}$ and is consistent with the results measured for jets using 2015 Pb+Pb data [23].

The R_{AA} is observed to depend significantly on r_g, with a clear ordering with respect to the splitting angle. Jets that fail the soft-drop grooming procedure and having r_g values < 0.02 are observed to be the least suppressed with an R_{AA} value of ~0.75 in central Pb+Pb collisions. On the contrary, jets with the widest splitting angle between their hardest subjets are observed to be suppressed with an R_{AA} value of ~0.3. Notably, the difference in the R_{AA} values is the largest between jets having r_g values below and above 0.02, supporting a decoherence picture of jet quenching [38, 39]. The R_{AA} for jets in different r_g regions is observed to be flatter as a function of p_T^{jet} compared to the R_{AA} behavior for the inclusive jets, especially in more central collisions. The upward slope of the jet R_{AA} for inclusive jets as a function of p_T^{jet} may be explained as arising from the increasing collimation of the jets with increasing p_T^{jet}; jets with lower r_g are significantly less suppressed in Pb+Pb collisions compared to large r_g jets and they also contribute to a larger fraction of the inclusive jets with increasing p_T^{jet}, resulting in a rising trend for R_{AA} as a function of p_T^{jet}. As a function of r_g, R_{AA} decreases smoothly with increasing r_g (shown in logarithmic scale) in all centrality intervals and is again noted to not significantly depend on the p_T^{jet} in the measured kinematic range.

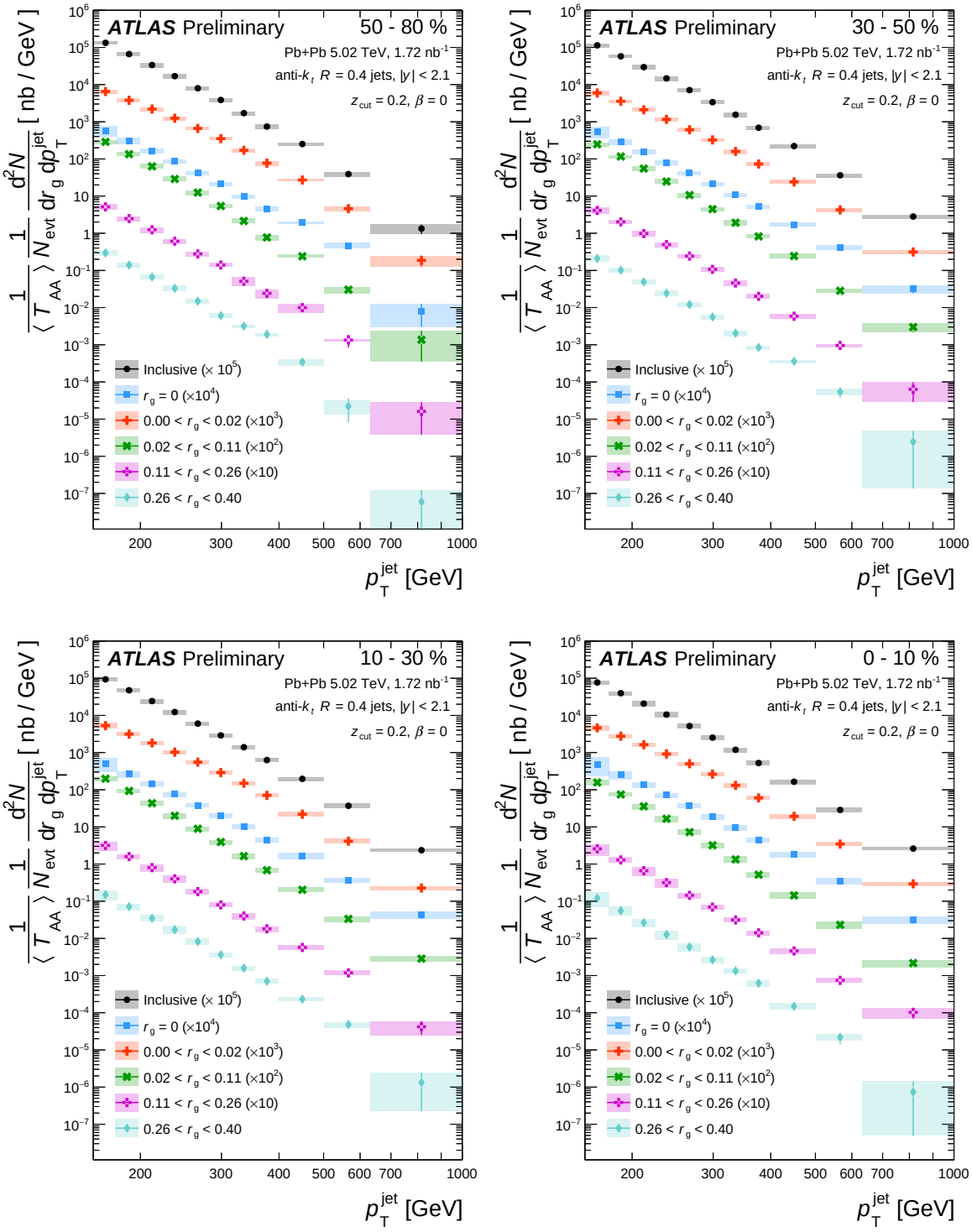

Figure 8: The per-event inclusive jet yield in Pb+Pb collisions at $\sqrt{s_{NN}}$ = 5.02 TeV normalized by $\langle T_{AA} \rangle$ as a function of p_T^{jet} in four centrality intervals. Distributions for inclusive jets (no grooming) and for those jets that fail the soft-drop requirement (r_g =0) are also shown. For each r_g interval, an additional scaling factor of 10 is applied to the plotted points for visual clarity. The statistical uncertainties are indicated by the error bars while the systematic uncertainties are indicated by the shaded bars. The normalization uncertainties on the $\langle T_{AA} \rangle$ for each centrality bin not shown. They are listed in Table 1.

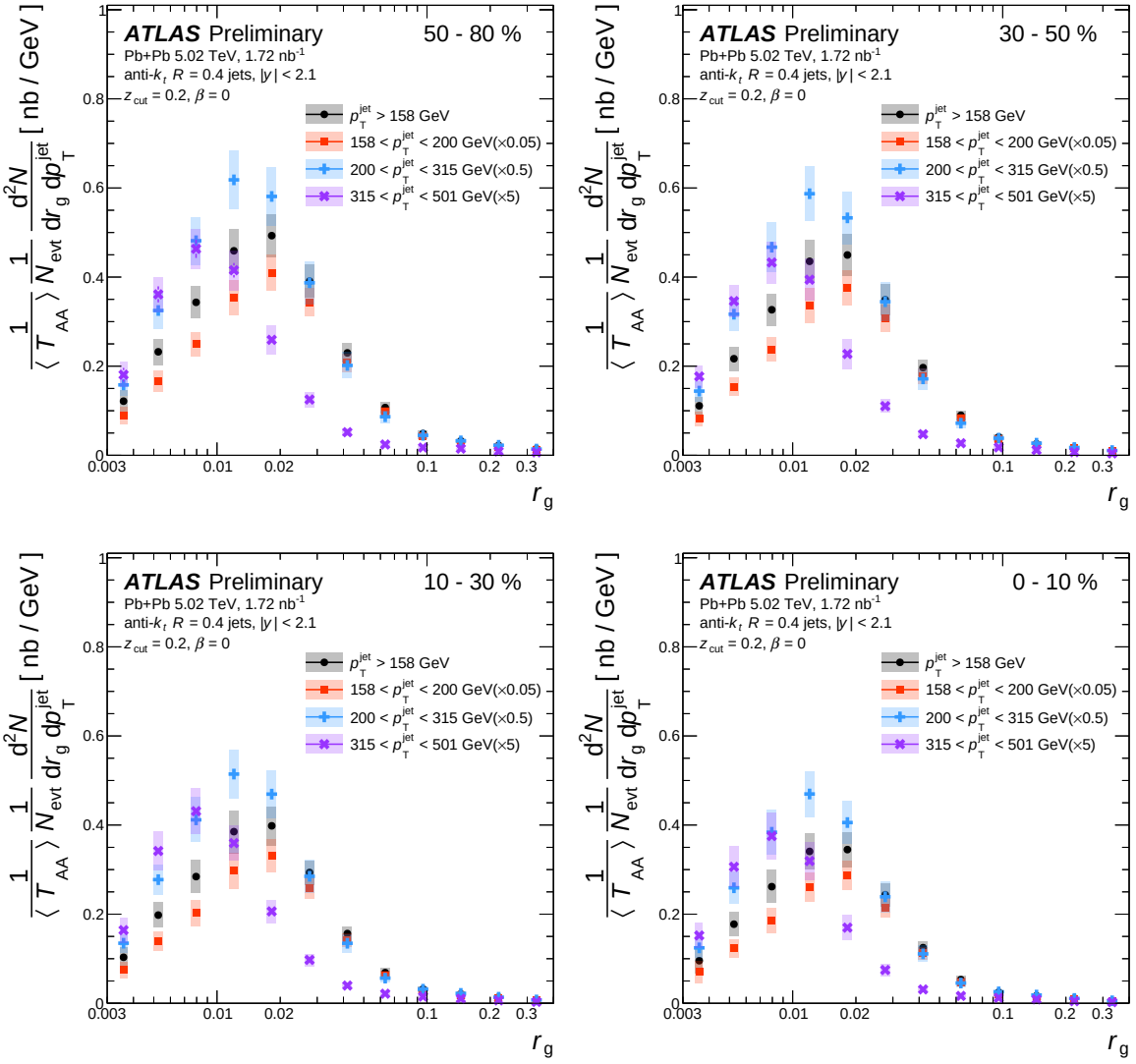

Figure 9: The per-event inclusive jet yield in Pb+Pb collisions at $\sqrt{s_{\mathrm{NN}}}$ = 5.02 TeV normalized by $\langle T_{\mathrm{AA}} \rangle$ as a function of soft-drop r_{g} in four centrality intervals and four $p_{\mathrm{T}}^{\mathrm{jet}}$ intervals as well for $p_{\mathrm{T}}^{\mathrm{jet}} > 158$ GeV. The statistical uncertainties are indicated by the error bars while the systematic uncertainties are indicated by the shaded bars. The normalization uncertainties on the $\langle T_{\mathrm{AA}} \rangle$ for each centrality bin not shown. They are listed in Table 1.

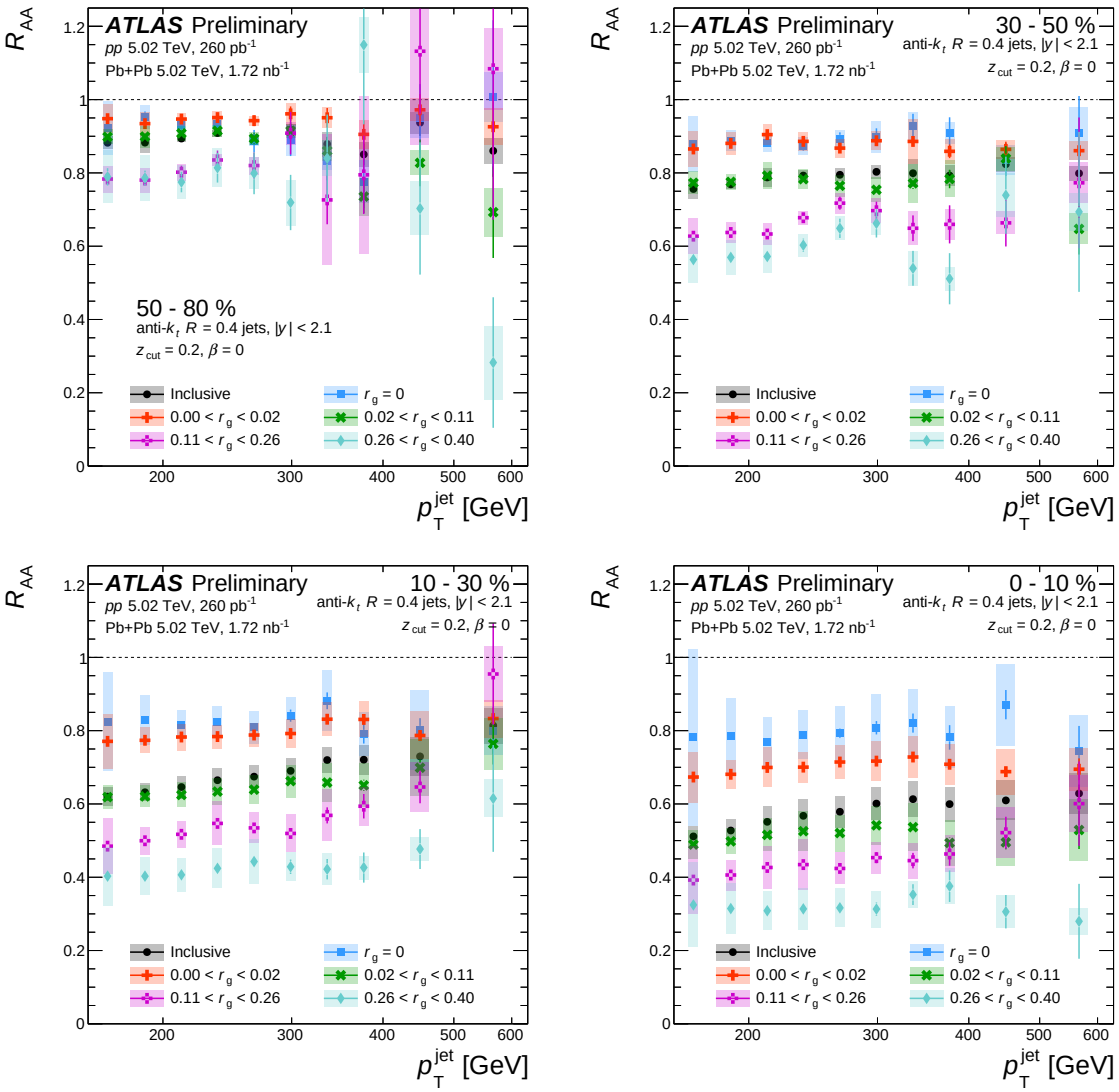

Figure 10: Nuclear modification factor, R_{AA}, as a function of $p_{\mathrm{T}}^{\mathrm{jet}}$ for soft-drop groomed jets with $|y| < 2.1$ in four centrality intervals and four intervals of r_{g}. Groomed jet R_{AA} values are compared to R_{AA} of jets without significant splitting identified by soft-drop procedure ($r_{\mathrm{g}} = 0$) and jets without grooming (inclusive). The error bars represent statistical uncertainties, the shaded bars around the data points represent bin-wise correlated systematic uncertainties. The global uncertainties on the normalization from the pp luminosity and $\langle T_{\mathrm{AA}} \rangle$ are not included. They are listed in Table 1.

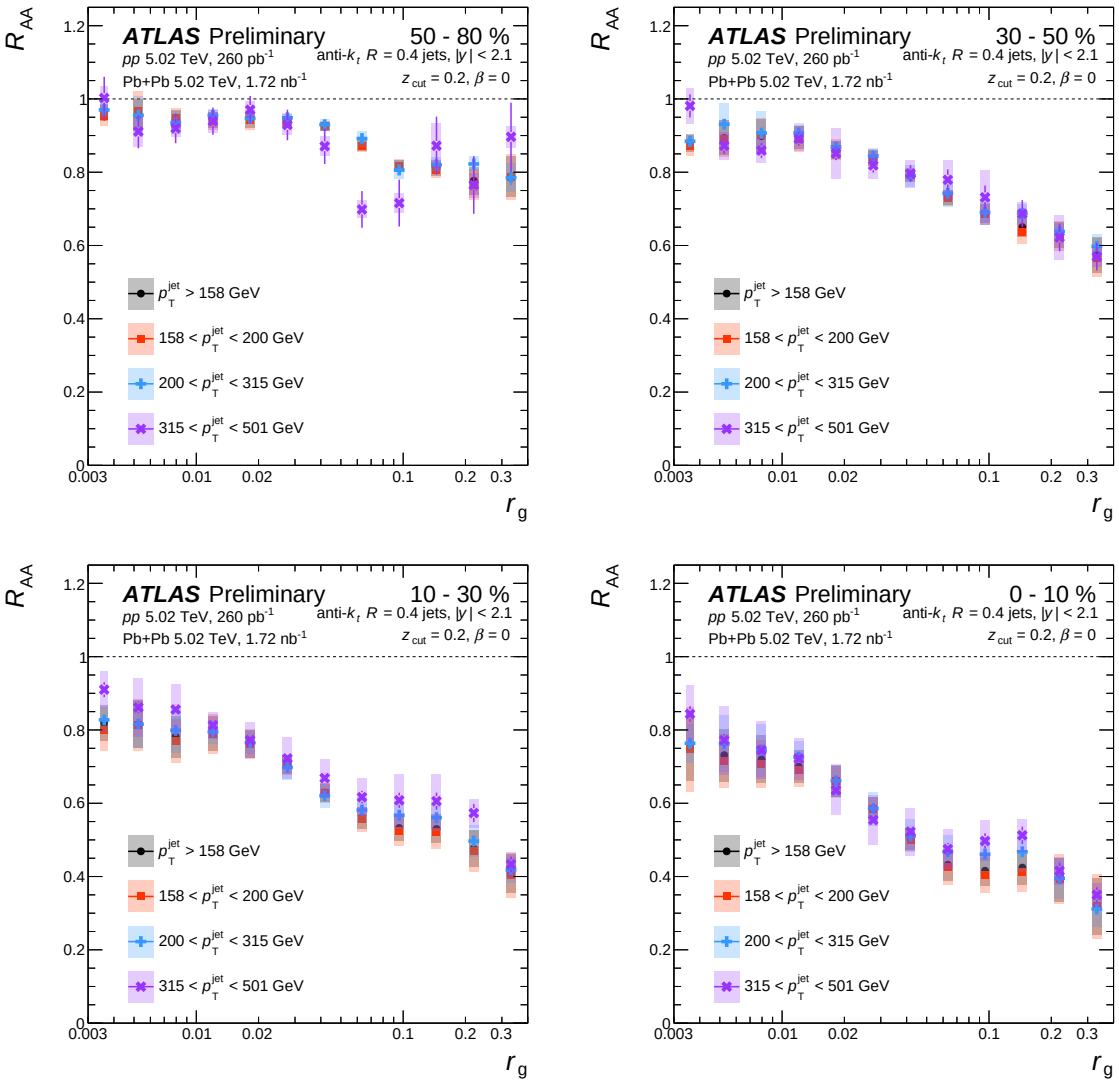

Figure 11: Nuclear modification factor, R_{AA}, as a function of r_{g} for soft-drop groomed jets with $|y| < 2.1$ in four centrality intervals and three intervals of $p_{\mathrm{T}}^{\mathrm{jet}}$, in comparison to the p_{T} integrated results. The error bars represent statistical uncertainties, the shaded bars around the data points represent bin-wise correlated systematic uncertainties. The global uncertainties on the normalization from the pp luminosity and $\langle T_{\mathrm{AA}} \rangle$ are not included. They are listed in Table 1.

7 Conclusion

Measurements of inclusive jet production in Pb+Pb and pp collisions are presented using integrated luminosities of 1.72 nb^{-1} and 260 pb^{-1}, respectively. The jets are reconstructed using the anti-k_t algorithm with $R = 0.4$ and groomed using the soft-drop procedure with parameters $z_{\text{cut}} = 0.2$ and $\beta = 0$. The jet differential cross-sections and yields are presented as a function of $p_{\text{T}}^{\text{jet}}$ and r_{g}, the opening angle of the hardest splitting, and in intervals of collision centrality. Results unfolded to the particle-level are presented for jets with $p_{\text{T}}^{\text{jet}} > 158$ GeV, $|y| < 2.1$, $0 \leq r_{\text{g}} < 0.4$.

The r_{g} distributions obtained in pp collisions are observed to peak at lower values of r_{g} with increasing $p_{\text{T}}^{\text{jet}}$, indicating that higher momentum jets are more collimated. The differential cross-sections as a function of $p_{\text{T}}^{\text{jet}}$ and r_{g} are compared to results of MC event generators (Pythia8, Herwig and Sherpa), with the Pythia8 predictions showing the best agreement with the data, both in terms of the overall normalization and the differential cross-sections as a function of $p_{\text{T}}^{\text{jet}}$ and r_{g}.

The jet energy loss and the resulting suppression in Pb+Pb < is quantified by the nuclear modification factor, R_{AA}. The magnitude of the R_{AA} is observed to depend primarily on r_{g} of the jet and on the event centrality. In the most central collisions, the R_{AA} ranges between $R_{\text{AA}} \sim 0.75$ for the most collimated jets (r_{g}<0.02) to $R_{\text{AA}} \sim 0.3$ for the widest jets ($0.26 < r_{\text{g}} < 0.4$). The R_{AA} is observed to decrease monotonically with increasing r_{g}, and does not depend strongly on $p_{\text{T}}^{\text{jet}}$ for a given value of r_{g}. Although the energy loss is not measured directly and must be inferred from the R_{AA} and slope of the $p_{\text{T}}^{\text{jet}}$ distributions, the $p_{\text{T}}^{\text{jet}}$ dependence is observed to be similar for different r_{g} ranges. These features together with the dependence of the R_{AA} on r_{g} indicates that jets with larger opening angles lose more energy. The results presented here are qualitatively consistent with a picture of jet quenching dictated by coherence and provide the most direct evidence so far supporting this approach.

References

[1] STAR Collaboration, *Experimental and theoretical challenges in the search for the quark gluon plasma: The STAR Collaboration's critical assessment of the evidence from RHIC collisions*, Nucl. Phys. A **757** (2005) 102, arXiv: nucl-ex/0501009 (cit. on p. 2).

[2] PHENIX Collaboration, *Formation of dense partonic matter in relativistic nucleus-nucleus collisions at RHIC: Experimental evaluation by the PHENIX collaboration*, Nucl. Phys. A **757** (2005) 184, arXiv: nucl-ex/0410003 (cit. on p. 2).

[3] M. Gyulassy and L. McLerran, *New forms of QCD matter discovered at RHIC*, Nucl. Phys. A **750** (2005) 30, ed. by D. Rischke and G. Levin, arXiv: nucl-th/0405013 (cit. on p. 2).

[4] W. Busza, K. Rajagopal and W. van der Schee, *Heavy Ion Collisions: The Big Picture, and the Big Questions*, Ann. Rev. Nucl. Part. Sci. **68** (2018) 339, arXiv: 1802.04801 [hep-ph] (cit. on p. 2).

[5] M. Gyulassy and M. Plumer, *Jet Quenching in Dense Matter*, Phys. Lett. B **243** (1990) 432 (cit. on p. 2).

[6] J. D. Bjorken, *Energy Loss of Energetic Partons in Quark - Gluon Plasma: Possible Extinction of High p(t) Jets in Hadron - Hadron Collisions*, FERMILAB-PUB-82-059-THY (1982) (cit. on p. 2).

[7] D. Krohn, J. Thaler and L.-T. Wang, *Jet Trimming*, JHEP **02** (2010) 084, arXiv: 0912.1342 [hep-ph] (cit. on p. 2).

[8] M. Dasgupta, A. Fregoso, S. Marzani and G. P. Salam, *Towards an understanding of jet substructure*, JHEP **09** (2013) 029, arXiv: 1307.0007 [hep-ph] (cit. on pp. 2, 7).

[9] A. J. Larkoski, S. Marzani, G. Soyez and J. Thaler, *Soft Drop*, JHEP **05** (2014) 146, arXiv: 1402.2657 [hep-ph] (cit. on pp. 2, 7).

[10] ATLAS Collaboration, *Measurement of the Soft-Drop Jet Mass in pp Collisions at $\sqrt{s} = 13$ TeV with the ATLAS detector*, Phys. Rev. Lett. **121** (2018) 092001, arXiv: 1711.08341 [hep-ex] (cit. on pp. 2, 6).

[11] ATLAS Collaboration, *Measurement of soft-drop jet observables in pp collisions with the ATLAS detector at $\sqrt{s} = 13$ TeV*, Phys. Rev. D **101** (2020) 052007, arXiv: 1912.09837 [hep-ex] (cit. on pp. 2, 6, 10, 11).

[12] Y. Mehtar-Tani and K. Tywoniuk, *Groomed jets in heavy-ion collisions: sensitivity to medium-induced bremsstrahlung*, JHEP **04** (2017) 125, arXiv: 1610.08930 [hep-ph] (cit. on pp. 2, 3).

[13] Y.-T. Chien and I. Vitev, *Probing the Hardest Branching within Jets in Heavy-Ion Collisions*, Phys. Rev. Lett. **119** (2017) 112301, arXiv: 1608.07283 [hep-ph] (cit. on p. 2).

[14] H. A. Andrews et al., *Novel tools and observables for jet physics in heavy-ion collisions*, J. Phys. G **47** (2020) 065102, arXiv: 1808.03689 [hep-ph] (cit. on p. 2).

[15] CMS Collaboration, *Measurement of the Splitting Function in pp and PbPb collisions at $\sqrt{s_{NN}} = 5.02$ TeV*, Phys. Rev. Lett. **120** (2018) 142302, arXiv: 1708.09429 [hep-ex] (cit. on pp. 2, 7).

[16] CMS Collaboration, *Measurement of the groomed jet mass in PbPb and pp collisions at $\sqrt{s_{NN}} = 5.02$ TeV*, JHEP **10** (2018) 161, arXiv: 1805.05145 [hep-ex] (cit. on pp. 2, 7).

[17] ALICE Collaboration, *Exploration of jet substructure using iterative declustering in pp and Pb–Pb collisions at LHC energies*, Phys. Lett. B **802** (2020) 135227, arXiv: 1905.02512 [nucl-ex] (cit. on pp. 2, 7).

[18] ALICE Collaboration, *Measurement of the groomed jet radius and momentum splitting fraction in pp and Pb−Pb collisions at $\sqrt{s_{\mathrm{NN}}} = 5.02$ TeV*, (2021), arXiv: 2107.12984 [nucl-ex] (cit. on p. 2).

[19] P. Foka and M. A. Janik, *An overview of experimental results from ultra-relativistic heavy-ion collisions at the CERN LHC: Hard probes*, Rev. Phys. **1** (2016) 172, arXiv: 1702.07231 [hep-ex] (cit. on p. 2).

[20] L. Cunqueiro and A. M. Sickles, *Studying the QGP with Jets at the LHC and RHIC*, Progress in Particle and Nuclear Physics **124** (2022) 103940, arXiv: 2110.14490 [nucl-ex] (cit. on p. 2).

[21] ATLAS Collaboration, *Measurement of the jet radius and transverse momentum dependence of inclusive jet suppression in lead–lead collisions at $\sqrt{s_{NN}} = 2.76$ TeV with the ATLAS detector*, Phys. Lett. B **719** (2013) 220, arXiv: 1208.1967 [hep-ex] (cit. on pp. 2, 3).

[22] ATLAS Collaboration, *Measurements of the Nuclear Modification Factor for Jets in Pb+Pb Collisions at* $\sqrt{s_{NN}} = 2.76$ *TeV with the ATLAS Detector*, Phys. Rev. Lett. **114** (2015) 072302, arXiv: 1411.2357 [hep-ex] (cit. on p. 2).

[23] ATLAS Collaboration, *Measurement of the nuclear modification factor for inclusive jets in Pb+Pb collisions at* $\sqrt{s_{NN}} = 5.02$ *TeV with the ATLAS detector*, Phys. Lett. B **790** (2019) 108, arXiv: 1805.05635 [hep-ex] (cit. on pp. 2, 5, 6, 15).

[24] CMS Collaboration, *Measurement of inclusive jet cross-sections in pp and PbPb collisions at* $\sqrt{s_{NN}} = 2.76$ *TeV*, Phys. Rev. C **96** (2017) 015202, arXiv: 1609.05383 [hep-ex] (cit. on p. 2).

[25] ATLAS Collaboration, *Observation of a Centrality-Dependent Dijet Asymmetry in Lead–Lead Collisions at* $\sqrt{s_{NN}} = 2.76$ *TeV with the ATLAS Detector at the LHC*, Phys. Rev. Lett. **105** (2010) 252303, arXiv: 1011.6182 [hep-ex] (cit. on p. 2).

[26] ATLAS Collaboration, *Measurement of photon-jet transverse momentum correlations in* 5.02 *TeV Pb+Pb and pp collisions with ATLAS*, Phys. Lett. B **789** (2019) 167, arXiv: 1809.07280 [hep-ex] (cit. on pp. 2, 4, 5).

[27] CMS Collaboration, *In-medium modification of dijets in PbPb collisions at* $\sqrt{s_{NN}} = 5.02$ *TeV*, JHEP **05** (2021) 116, arXiv: 2101.04720 [hep-ex] (cit. on p. 2).

[28] CMS Collaboration, *Study of jet quenching with Z+jet correlations in PbPb and pp collisions at* $\sqrt{s_{NN}} = 5.02$ *TeV*, Phys. Rev. Lett. **119** (2017) 082301, arXiv: 1702.01060 [hep-ex] (cit. on p. 2).

[29] ATLAS Collaboration, *Measurement of jet fragmentation in Pb+Pb and pp collisions at* $\sqrt{s_{NN}} = 5.02$ *TeV with the ATLAS detector*, Phys. Rev. C **98** (2018) 024908, arXiv: 1805.05424 [hep-ex] (cit. on pp. 2, 6, 10, 29, 30).

[30] ATLAS Collaboration, *Comparison of Fragmentation Functions for Jets Dominated by Light Quarks and Gluons from pp and Pb+Pb Collisions in ATLAS*, Phys. Rev. Lett. **123** (2019) 042001, arXiv: 1902.10007 [hep-ex] (cit. on p. 2).

[31] CMS Collaboration, *Measurement of jet fragmentation in PbPb and pp collisions at* $\sqrt{s_{NN}} = 2.76$ *TeV*, Phys. Rev. C **90** (2014) 024908, arXiv: 1406.0932 [hep-ex] (cit. on p. 2).

[32] CMS Collaboration, *Observation of Medium Induced Modifications of Jet Fragmentation in PbPb Collisions at* $\sqrt{s_{NN}} = 5.02$ *TeV Using Isolated Photon-Tagged Jets*, Phys. Rev. Lett. **121** (2018) 242301, arXiv: 1801.04895 [hep-ex] (cit. on p. 2).

[33] STAR Collaboration, *Measurement of groomed jet substructure observables in p+p collisions at* $\sqrt{s}$ *=200 GeV with STAR*, Phys. Lett. B **811** (2020) 135846, arXiv: 2003.02114 [hep-ex] (cit. on pp. 2, 7).

[34] Y. L. Dokshitzer, V. A. Khoze, S. I. Troian and A. H. Mueller, *QCD Coherence in High-Energy Reactions*, Rev. Mod. Phys. **60** (1988) 373 (cit. on p. 3).

[35] R. Baier, Y. L. Dokshitzer, A. H. Mueller, S. Peigne and D. Schiff, *Radiative energy loss of high-energy quarks and gluons in a finite volume quark - gluon plasma*, Nucl. Phys. B **483** (1997) 291, arXiv: hep-ph/9607355 [hep-ph] (cit. on p. 3).

[36] J. Casalderrey-Solana, Y. Mehtar-Tani, C. A. Salgado and K. Tywoniuk, *New picture of jet quenching dictated by color coherence*, Phys. Lett. B **725** (2013) 357, arXiv: 1210.7765 [hep-ph] (cit. on p. 3).

[37] G. Milhano, U. A. Wiedemann and K. C. Zapp,
Sensitivity of jet substructure to jet-induced medium response, Phys. Lett. B **779** (2018) 409,
arXiv: 1707.04142 [hep-ph] (cit. on p. 3).

[38] P. Caucal, E. Iancu and G. Soyez,
Deciphering the z_g distribution in ultrarelativistic heavy ion collisions, JHEP **10** (2019) 273,
arXiv: 1907.04866 [hep-ph] (cit. on pp. 3, 6, 16, 27).

[39] P. Caucal, E. Iancu and G. Soyez, *Jet radiation in a longitudinally expanding medium*,
JHEP **04** (2021) 209, arXiv: 2012.01457 [hep-ph] (cit. on pp. 3, 6, 16, 27).

[40] M. Cacciari, G. P. Salam and G. Soyez, *The anti-k_t jet clustering algorithm*, JHEP **04** (2008) 063,
arXiv: 0802.1189 [hep-ph] (cit. on pp. 3, 5).

[41] ATLAS Collaboration, *The ATLAS Experiment at the CERN Large Hadron Collider*,
JINST **3** (2008) S08003 (cit. on p. 3).

[42] ATLAS Collaboration, *ATLAS Insertable B-Layer Technical Design Report*,
ATLAS-TDR-19; CERN-LHCC-2010-013, 2010,
URL: https://cds.cern.ch/record/1291633 (cit. on p. 3),
Addendum: ATLAS-TDR-19-ADD-1; CERN-LHCC-2012-009, 2012, URL:
https://cds.cern.ch/record/1451888.

[43] B. Abbott et al., *Production and integration of the ATLAS Insertable B-Layer*,
JINST **13** (2018) T05008, arXiv: 1803.00844 [physics.ins-det] (cit. on p. 3).

[44] ATLAS Collaboration, *Performance of the ATLAS trigger system in 2015*,
Eur. Phys. J. C **77** (2017) 317, arXiv: 1611.09661 [hep-ex] (cit. on p. 4).

[45] ATLAS Collaboration, *The ATLAS Collaboration Software and Firmware*,
ATL-SOFT-PUB-2021-001, 2021, URL: https://cds.cern.ch/record/2767187 (cit. on p. 4).

[46] ATLAS Collaboration, *ATLAS data quality operations and performance for 2015–2018 data-taking*,
JINST **15** (2020) P04003, arXiv: 1911.04632 [physics.ins-det] (cit. on p. 4).

[47] ATLAS Collaboration, *Measurement of azimuthal anisotropy of muons from charm and bottom hadrons in Pb+Pb collisions at $\sqrt{s_{NN}} = 5.02$ TeV with the ATLAS detector*,
Phys. Lett. B **807** (2020) 135595, arXiv: 2003.03565 [hep-ex] (cit. on p. 4).

[48] M. L. Miller, K. Reygers, S. J. Sanders and P. Steinberg,
Glauber modeling in high energy nuclear collisions, Ann. Rev. Nucl. Part. Sci. **57** (2007) 205,
arXiv: nucl-ex/0701025 [nucl-ex] (cit. on p. 4).

[49] C. Loizides, J. Nagle and P. Steinberg, *Improved version of the PHOBOS Glauber Monte Carlo*,
SoftwareX **1-2** (2015) 13, arXiv: 1408.2549 [nucl-ex] (cit. on p. 4).

[50] ATLAS Collaboration, *Measurement of $W^{\pm}$ boson production in Pb+Pb collisions at $\sqrt{s_{NN}} = 5.02$ TeV with the ATLAS detector*, Eur. Phys. J. C **79** (2019) 935,
arXiv: 1907.10414 [hep-ex] (cit. on p. 4).

[51] T. Sjöstrand et al., *An introduction to PYTHIA 8.2*, Comput. Phys. Commun. **191** (2015) 159,
arXiv: 1410.3012 [hep-ph] (cit. on p. 4).

[52] ATLAS Collaboration, *ATLAS Pythia 8 tunes to 7 TeV data*, ATL-PHYS-PUB-2014-021, 2014,
URL: https://cds.cern.ch/record/1966419 (cit. on p. 4).

[53] S. Agostinelli et al., *Geant4—a simulation toolkit*, Nuclear Instruments and Methods in Physics Research Section A: Accelerators, Spectrometers, Detectors and Associated Equipment **506** (2003) 250, ISSN: 0168-9002 (cit. on p. 5).

[54] ATLAS Collaboration, *Measurements of azimuthal anisotropies of jet production in Pb+Pb collisions at $\sqrt{s_{NN}}$ = 5.02 TeV with the ATLAS detector*, (2021), arXiv: 2111.06606 [nucl-ex] (cit. on pp. 5, 7).

[55] M. Cacciari, G. P. Salam and G. Soyez, *FastJet user manual*, Eur. Phys. J. C **72** (2012) 1896, arXiv: 1111.6097 [hep-ph] (cit. on p. 5).

[56] ATLAS Collaboration, *Jet energy measurement with the ATLAS detector in proton–proton collisions at $\sqrt{s}$ = 7 TeV*, Eur. Phys. J. C **73** (2013) 2304, arXiv: 1112.6426 [hep-ex] (cit. on pp. 5, 10).

[57] ATLAS Collaboration, *Measurement of the azimuthal anisotropy of charged particles produced in $\sqrt{s_{NN}}$ = 5.02 TeV Pb+Pb collisions with the ATLAS detector*, Eur. Phys. J. C **78** (2018) 997, arXiv: 1808.03951 [hep-ex] (cit. on pp. 5, 11).

[58] ATLAS Collaboration, *Jet energy scale and its uncertainty for jets reconstructed using the ATLAS heavy ion jet algorithm*, ATLAS-CONF-2015-016, 2015, URL: https://cds.cern.ch/record/2008677 (cit. on pp. 5, 10).

[59] ATLAS Collaboration, *Topological cell clustering in the ATLAS calorimeters and its performance in LHC Run 1*, Eur. Phys. J. C **77** (2017) 490, arXiv: 1603.02934 [hep-ex] (cit. on p. 6).

[60] ATLAS Collaboration, *Improving jet substructure performance in ATLAS using Track-CaloClusters*, ATL-PHYS-PUB-2017-015, 2017, URL: https://cds.cern.ch/record/2275636 (cit. on pp. 6, 14).

[61] ATLAS Collaboration, *A W/Z-boson tagger using Track-CaloCluster jets with ATLAS*, ATL-PHYS-PUB-2020-008, 2020, URL: https://cds.cern.ch/record/2718218 (cit. on p. 6).

[62] ATLAS Collaboration, *Jet reconstruction and performance using particle flow with the ATLAS Detector*, Eur. Phys. J. C **77** (2017) 466, arXiv: 1703.10485 [hep-ex] (cit. on p. 6).

[63] ATLAS Collaboration, *Optimisation of large-radius jet reconstruction for the ATLAS detector in 13 TeV proton–proton collisions*, Eur. Phys. J. C **81** (2020) 334, arXiv: 2009.04986 [hep-ex] (cit. on p. 6).

[64] ATLAS Collaboration, *Performance of the ATLAS track reconstruction algorithms in dense environments in LHC Run 2*, Eur. Phys. J. C **77** (2017) 673, arXiv: 1704.07983 [hep-ex] (cit. on pp. 6, 11).

[65] ATLAS Collaboration, *Measurement of charged-particle spectra in Pb+Pb collisions at $\sqrt{s_{NN}}$ = 2.76 TeV with the ATLAS detector at the LHC*, JHEP **09** (2015) 050, arXiv: 1504.04337 [hep-ex] (cit. on p. 6).

[66] M. Wobisch and T. Wengler, 'Hadronization corrections to jet cross-sections in deep inelastic scattering', *Workshop on Monte Carlo Generators for HERA Physics (Plenary Starting Meeting)*, 1998 270, arXiv: hep-ph/9907280 (cit. on p. 7).

[67] Y. L. Dokshitzer, G. D. Leder, S. Moretti and B. R. Webber, *Better jet clustering algorithms*, JHEP **08** (1997) 001, arXiv: hep-ph/9707323 (cit. on p. 7).

[68] T. Adye, 'Unfolding algorithms and tests using RooUnfold', *Proceedings, 2011 Workshop on Statistical Issues Related to Discovery Claims in Search Experiments and Unfolding (PHYSTAT 2011)* (CERN, Geneva, Switzerland, 17th–20th Jan. 2011) 313, arXiv: 1105.1160 [physics.data-an] (cit. on pp. 8, 11).

[69] G. D'Agostini, *A multidimensional unfolding method based on Bayes' theorem*, Nucl. Instrum. Meth. A **362** (1995) 487, ISSN: 0168-9002 (cit. on p. 9).

[70] ATLAS Collaboration, *Jet energy scale measurements and their systematic uncertainties in proton–proton collisions at $\sqrt{s}$ = 13 TeV with the ATLAS detector*, Phys. Rev. D **96** (2017) 072002, arXiv: 1703.09665 [hep-ex] (cit. on p. 10).

[71] ATLAS Collaboration, *Jet energy resolution in proton–proton collisions at $\sqrt{s}$ = 7 TeV recorded in 2010 with the ATLAS detector*, Eur. Phys. J. C **73** (2013) 2306, arXiv: 1210.6210 [hep-ex] (cit. on p. 10).

[72] ATLAS Collaboration, *Measurements of jet vetoes and azimuthal decorrelations in dijet events produced in pp collisions at $\sqrt{s}$ = 7 TeV using the ATLAS detector*, Eur. Phys. J. C **74** (2014) 3117, arXiv: 1407.5756 [hep-ex] (cit. on p. 11).

[73] ATLAS Collaboration, *Study of the material of the ATLAS inner detector for Run 2 of the LHC*, JINST **12** (2017) P12009, arXiv: 1707.02826 [hep-ex] (cit. on p. 11).

[74] ATLAS Collaboration, *Measurement of track reconstruction inefficiencies in the core of jets via pixel dE/dx with the ATLAS experiment using $\sqrt{s}$ = 13 TeV pp collision data*, ATL-PHYS-PUB-2016-007, 2016, URL: https://cds.cern.ch/record/2140460 (cit. on p. 11).

[75] G. Avoni et al., *The new LUCID-2 detector for luminosity measurement and monitoring in ATLAS*, JINST **13** (2018) P07017 (cit. on p. 11).

[76] ATLAS Collaboration, *Luminosity determination in pp collisions at $\sqrt{s}$ = 13 TeV using the ATLAS detector at the LHC*, ATLAS-CONF-2019-021, 2019, URL: https://cds.cern.ch/record/2677054 (cit. on p. 11).

[77] J. Bellm et al., *Herwig 7.1 Release Note*, (2017), arXiv: 1705.06919 [hep-ph] (cit. on p. 14).

[78] R. D. Ball et al., *Parton distributions for the LHC run II*, JHEP **04** (2015) 040, arXiv: 1410.8849 [hep-ph] (cit. on p. 14).

[79] E. Bothmann et al., *Event generation with Sherpa 2.2*, SciPost Phys. **7** (2019) 034, arXiv: 1905.09127 [hep-ph] (cit. on p. 14).

[80] S. Schumann and F. Krauss, *A parton shower algorithm based on Catani–Seymour dipole factorisation*, JHEP **03** (2008) 038, arXiv: 0709.1027 [hep-ph] (cit. on p. 14).

[81] CMS Collaboration, *Jet properties in PbPb and pp collisions at $\sqrt{s_{NN}}$ = 5.02 TeV*, JHEP **05** (2018) 006, arXiv: 1803.00042 [hep-ex] (cit. on pp. 29, 30).

Appendix

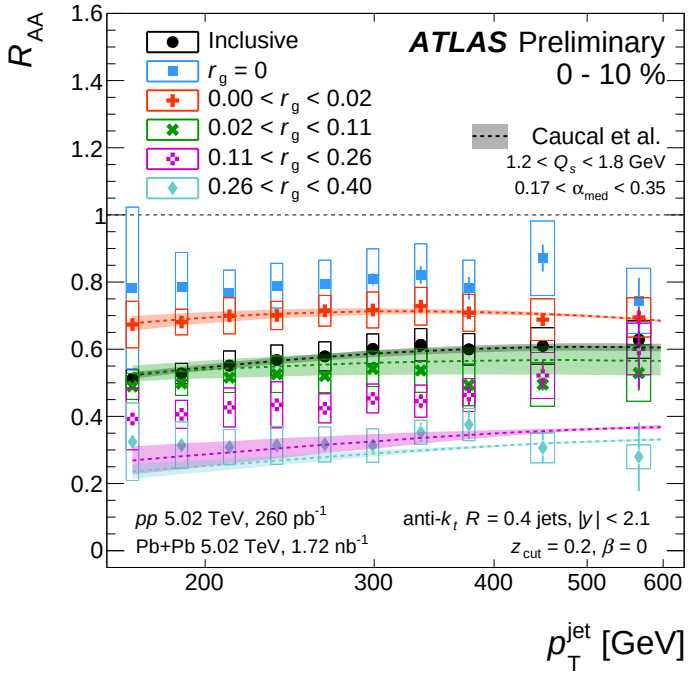

Figure 12: Comparison of R_{AA} for inclusive jets and for four intervals of r_g in $0-10\%$ centrality Pb+Pb events to theoretical predictions from the pQCD framework described in Refs. [38, 39]. The error bars and the open boxes around the data points represent the statistical and systematic uncertainties, respectively. The global uncertainties on the pp luminosity is 1.6% and on the $\langle T_{AA} \rangle$ for each centrality bin are listed in Table 1.

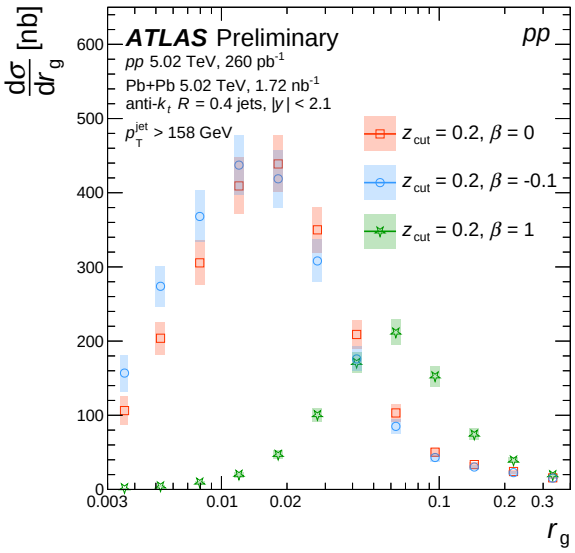

Figure 13: Inclusive cross-section of jets passing soft-drop grooming condition with $z_{\text{cut}} = 0.2$ and different β parameters (see Eq. 1) in pp collisions at $\sqrt{s} = 5.02$ TeV as a function of r_{g}. The error bars represent statistical uncertainties and shaded boxes represent systematic uncertainties. The global uncertainty on the pp luminosity is 1.6%. The r_{g} distribution for $\beta = 1$ is shifted to the right compared to $\beta = 0$ as increasing β values relaxes the threshold (see Eq. 1) to be satisfied with decreasing r_{g} and selects relatively more imbalanced subjets in the soft-drop procedure. Consequently, soft wide-angle radiation plays a more significant role in selecting subjets using $\beta = 1$ compared to $\beta = 0$ soft-drop condition. Conversely, $\beta = -0.1$ preferentially selects more balanced subjets compared to the $\beta = 0$ soft-drop condition with decreasing r_{g}.

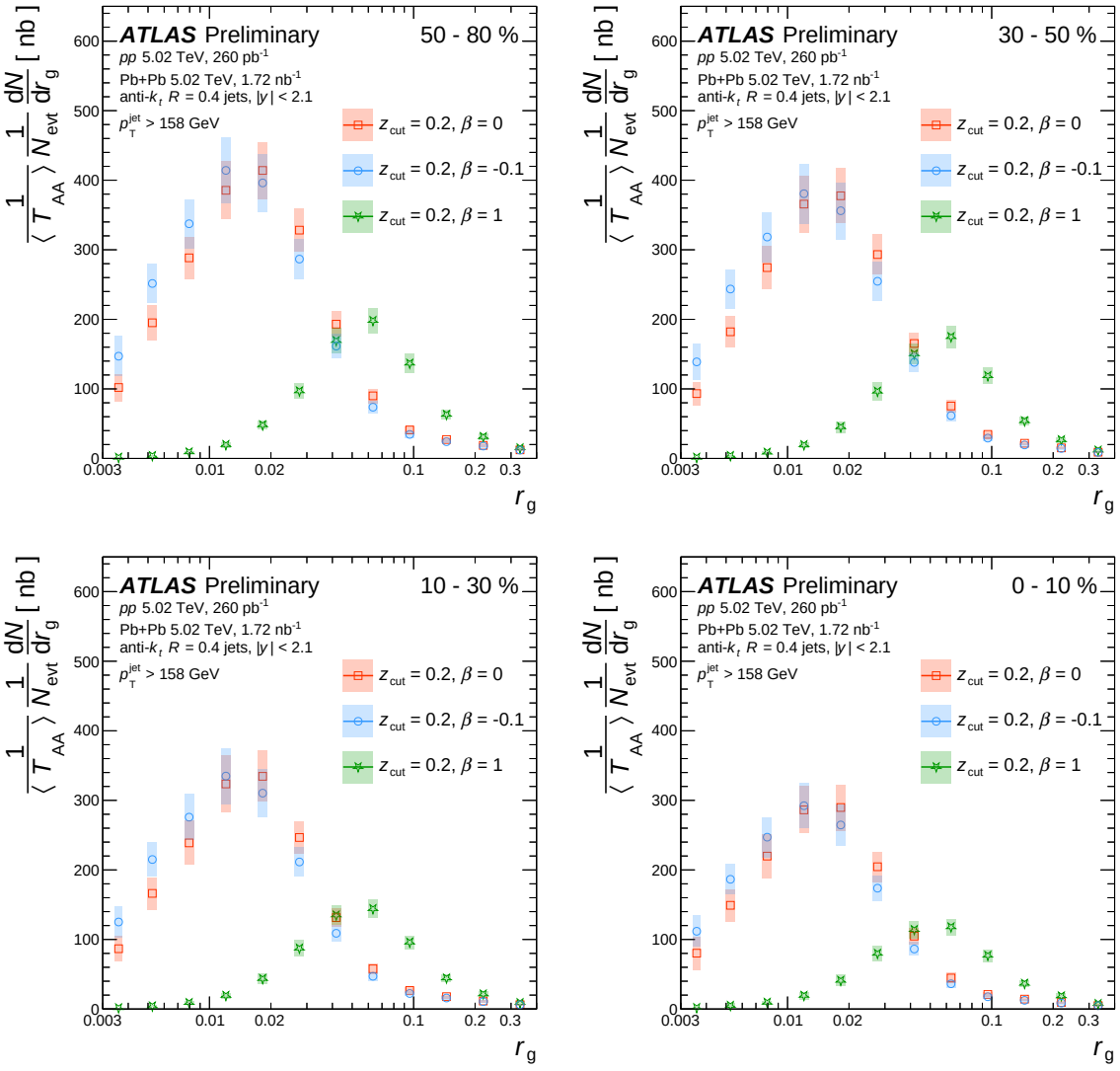

Figure 14: The per-event inclusive jet yield in Pb+Pb collisions at $\sqrt{s_{\mathrm{NN}}} = 5.02$ TeV normalized by $\langle T_{\mathrm{AA}} \rangle$ as a function of soft-drop r_{g} in four centrality intervals, with $z_{\mathrm{cut}} = 0.2$ and different β parameters (see Eq. 1). The error bars represent statistical uncertainties, shaded boxes represent systematic uncertainties. The global uncertainties on the $\langle T_{\mathrm{AA}} \rangle$ for each centrality bin are listed in Table 1. Similar to pp results, the r_{g} distributions for $\beta = 1$ is shifted to the right compared to $\beta = 0$ as increasing β values relaxes the threshold (see Eq. 1) to be satisfied with decreasing r_{g} and selects relatively more imbalanced subjets in the soft-drop procedure. Consequently, soft wide-angle radiation plays a more significant role in selecting subjets using $\beta = 1$ compared to $\beta = 0$ soft-drop condition. However, in Pb+Pb collisions, the soft wide-angle radiation has been observed to be significantly modified [29, 81], and this affects the properties of subjets being selected in Pb+Pb compared to pp collisions. Conversely, $\beta = -0.1$ preferentially selects more balanced subjets compared to the $\beta = 0$ soft-drop condition with decreasing r_{g}.

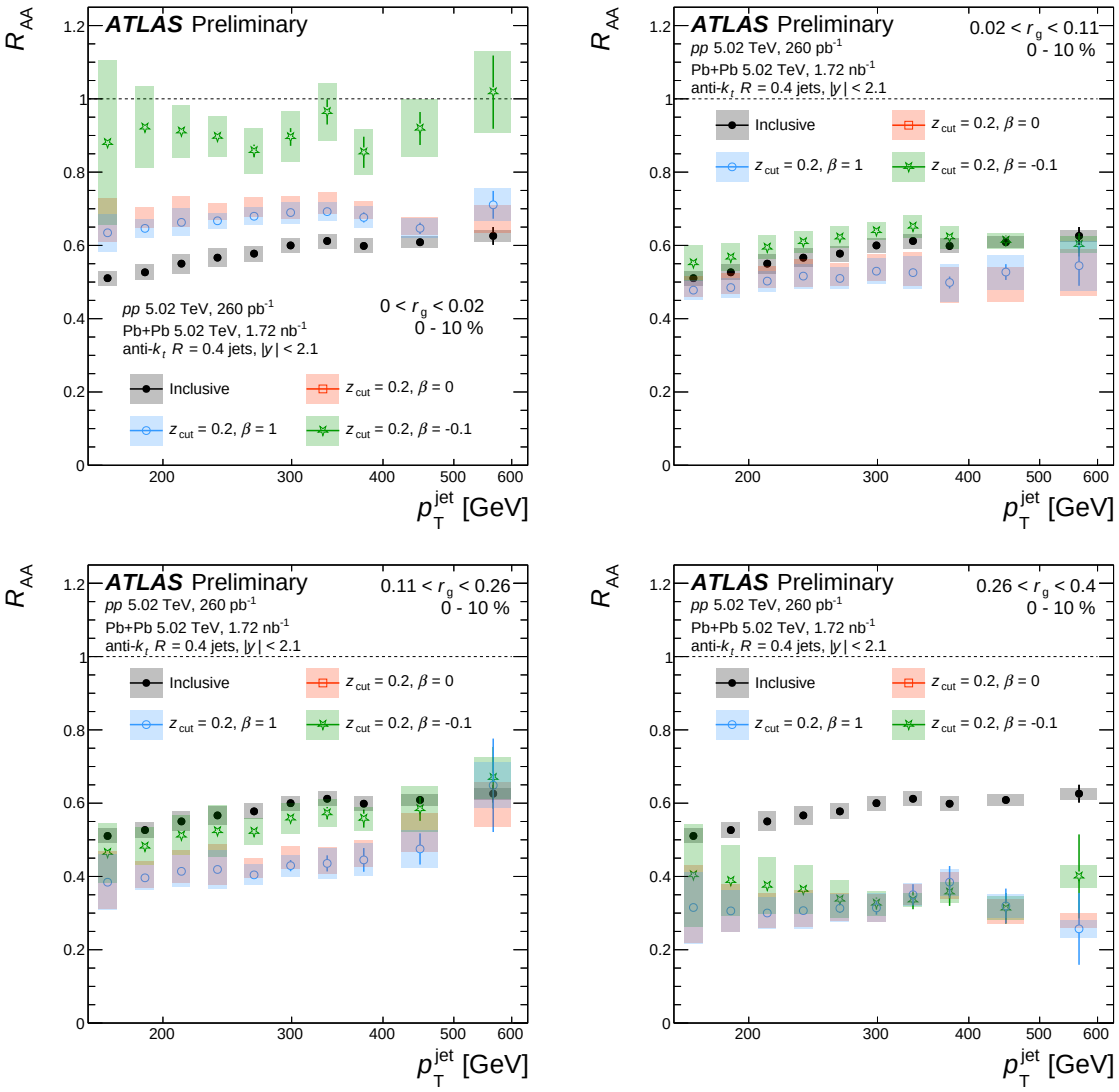

Figure 15: Nuclear modification factor, R_{AA}, as a function of $p_{\mathrm{T}}^{\mathrm{jet}}$ for soft-drop groomed jets with $z_{\mathrm{cut}} = 0.2$ and different β parameters (see Eq. 1) in $0-10\%$ centrality interval and for four different intervals of r_{g}. Groomed jet R_{AA} values are compared to R_{AA} of jets without grooming (inclusive). The error bars represent statistical uncertainties, the shaded boxes around the data points represent bin-wise correlated systematic uncertainties. The global uncertainties on the pp luminosity is 1.6% and on the $\langle T_{\mathrm{AA}} \rangle$ for each centrality bin are listed in Table 1. The R_{AA} values measured using $\beta = -0.1$ soft-drop parameter are in agreement with the nominal $\beta = 0$ results within systematic uncertainties, indicating that the dense environment of the jet core does not have a significant impact on identifying collimated symmetric subjets using $\beta = 0$. The R_{AA} values measured using $\beta = 1$ deviate from the nominal $\beta = 0$ results increasingly with decreasing r_{g}, resulting from a significant modification of the softer wide-angle radiation in jets measured in Pb+Pb collisions compared to those in pp [29, 81].